Geomorphic expressions of collisional tectonics in the Qilian Shan, north eastern Tibetan Plateau

Katharine Groves[a], Christopher Saville[a], Martin Hurst[b], Stuart Jones[a], Shuguang Song[c], Mark B. Allen[a]

[a]Department of Earth Sciences, University of Durham, Durham, DH1 3LE, UK,

[b]School of Geographical and Earth Sciences, University of Glasgow, Glasgow G12 8QQ, UK,

[c]MOE Key Laboratory of Orogenic Belts and Crustal Evolution, School of Earth and Space Sciences, Peking University, Beijing, China

Corresponding author: Katharine Groves katharine.groves@durham.ac.uk

Highlights:

- We analyse tectonic geomorphology across the Qilian Shan
- Geomorphic indices correlate with models of an underlying detachment thrust
- Regional east-west precipitation gradient does not control landscape evolution

Abstract

The Qilian Shan, north eastern Tibetan Plateau, is an area of active deformation caused by convergence in the India-Eurasia collision zone. Geomorphic indices capture the landscape response to competition between tectonics and climate, reflecting the spatial distribution of erosion. We use geomorphic indices (hypsometric integral (HI), normalised channel steepness (k_{sn}), elevation-relief ratio (ZR) and surface roughness (SR)) to identify areas of active deformation and erosion, highlight landscape variations and we interpret the results for potential tectonic and climatic drivers. High HI (> 0.15), k_{sn} (> 100) and low ZR (< 2) occur in the hanging wall of thrust faults, consistent with active uplift of these structures. Relatively high HI (> 0.15) and k_{sn} (> 100) values in the eastern region are attributed

to thrust parallel rivers in this region excavating wide valleys between the faults. The east-west precipitation variation across the Qilian Shan (>500 mm/yr to <100 mm/yr) is not a first order control on the regional landscape. There is an abrupt northwards transition from low to high HI, k_{sn} and SR and high to low ZR partially coincident with the left-lateral Haiyuan Fault. We suggest that this transition is due to a difference in deep structure. A south-to-north transition from creeping to locked behaviour on an underlying detachment thrust has previously been suggested to occur along the intersection of this thrust detachment with the overlying Haiyuan Fault, providing a potential explanation for the location of the geomorphic change. Our results show these geomorphic indices to be sensitive to the underlying tectonic structure of the area. These methods could be applied to other fold-and-thrust belts and tectonic settings, to help understand the underlying structure, and the processes responsible for deformation.

Keywords: Qilian Shan; geomorphic indices; fold-and-thrust belts; landscape; tectonics; precipitation

1 – Introduction

1a Introduction

The India-Eurasia and Arabia-Eurasia collisions are by far the largest active continental collisions on Earth. Processes and structures vary among the fold-and-thrust belts produced by these collisions (Tapponnier et al., 2001; Poblet and Lisle, 2011; Royden et al., 2008; Lacombe and Bellahsen, 2016; Kapp and DeCelles, 2019). By studying such zones of active deformation, it is possible to understand continental tectonics in ways that are not possible in inactive regions. One method that can be used to gain insights into underlying tectonic structure is tectonic geomorphology: the analysis of landscapes to help understand the underlying tectonics. Landscapes are affected by tectonics,

climate, underlying lithology and surface processes and react to changes in these controls (Burbank and Anderson, 2001; Kirby and Whipple, 2012).

The geomorphic methods used in this study are the hypsometric integral (HI) which is the distribution of relief, normalised channel steepness (k_{sn}), surface roughness (SR) and the elevation-relief ratio (ZR) which highlights areas of high elevation and low relief. Geomorphic indices are powerful tools for analysing patterns in the landscape of fold-and-thrust belts and interpreting them with regard to tectonics. For example, studies identify patterns such as faults acting as major boundaries between high and low HI regions (Gao et al., 2016), high HI and normalised channel steepness in the hanging walls of thrust faults (Gao et al., 2016; Nennewitz et al., 2018), high HI and k_{sn} at the limit of seismogenic thrusting (Obaid and Allen, 2019), identification of a shear zone by identifying high concavity streams (Wobus et al., 2006) channel steepness identifying variations in rock uplift rates across a fault-bend fold (Kirby and Whipple, 2001); identification of incised valleys (Tejero et al., 2006) and correlation of high long-term erosion rates to high channel steepness (Wobus et al., 2006). The geomorphic indices may also identify features such as underlying changes in deformation, as well as variations between fault parallel and fault transverse valleys.

The Qilian Shan fold-and-thrust belt is used here as a case study for the use of tectonic geomorphology to study continental scale processes. The Qilian Shan is at the northern margin of the Tibetan Plateau and is considered to be the youngest area to have deformed within the plateau (Figure 1), currently absorbing ~20% of the active convergence and is therefore able to tell us about the effects of upward and outward growth of the orogenic plateau and large scale tectonic processes (Tapponnier et al. 1990; 2001; Meyer et al., 1998; Yin et al., 2008; Yuan et al., 2013; Zuza et al., 2018). It is therefore a good location for studying continental tectonics, and the development of intracontinental fold-and-thrust belts in particular. The structure of the Qilian Shan is broadly agreed to be divergent thrusts and a subdued interior, overlying a south-dipping detachment (Figure 1; Meyer et al., 1998; Allen et al., 2017; Cheng et al., 2019). Compressional deformation across the range is oblique (transpressional)

(Figure 2), expressed by strain partitioning on the thrust faults and the strike-slip Haiyuan Fault (Gaudemer et al., 1995; Zheng et al., 2013). Therefore the Qilian Shan is also important as a study area for understanding strain partitioning, its expression in the geomorphology, and how landscapes can be interpreted to understand the underlying structure.

We use tectonic geomorphology to study the landscape of the Qilian Shan and to assess the evidence for this structure. Identification of the tectonic controls using these methods could point the way for future studies to assess how structures and processes differ in other fold-and-thrust belts. Another driver for this study is to assess the role of precipitation on landscape evolution. The Qilian Shan has an along strike variation in precipitation of ~600 mm/yr in the east due to influence of the East Asian monsoon, to <100 mm/yr in the west (Hu et al., 2010; Geng et al., 2017; Figure 3), whereas most mountain belts show more variation across strike, in the form of orographic precipitation. As precipitation varies in a different direction to tectonics the Qilian Shan provides a good area to analyse the impact of precipitation relative to tectonics on landscape morphology. Catchment averaged precipitation in Hawaii was found to correlate with bedrock river incision rates by Ferrier et al. (2013), who postulated that this relationship would apply on a global scale. If a similar correlation applies to the Qilian Shan, it predicts that the range will exhibit higher SR and HI in the eastern region due to higher precipitation and therefore incision, with a gradual decrease to lower values SR and HI towards the west due to lower precipitation and therefore lower incision.

Studies which find rainfall to be a good predictor of erosion rates are based in regions of low tectonically-driven uplift, whereas studies in tectonically active regions suggest relief to be the best predictor of erosion rates (Henck et al., 2010). If the latter is the case there would be no relationship between the geomorphic index patterns, but high HI and SR would be concentrated in areas of active rock uplift. Wang et al (2019) found no correlation between k_{sn} and precipitation in the Qilian Shan at the scale of the main drainage basins. There is very little variation (< 10°) in mean annual temperature,

with temperatures decreasing with increasing elevation (Pan et al., 2010) but with no change east-west or north-south.

1b Background

The Tibetan Plateau and its margins, including the Himalayas, accommodate over 90% of the active India-Eurasia plate convergence (Wang et al., 2001). The timing, rate and pattern of uplift of the Plateau are subjects of intense research (Wang et al., 2014a). Models for growth include continuous lateral growth model (England and Houseman, 1989), stepwise growth (Tapponnier et al., 2001) and outward growth from central Tibet (Wang et al., 2014a). Models of lower crustal channel flow (Royden et al., 2008) predict crustal thickening and surface uplift without crustal shortening, focussed on eastern and south-eastern Tibet. Many studies have been carried out across the region, including the Qilian Shan, with the aim of constraining the timing of uplift, using approaches such as low temperature thermochronology, stable isotope-based palaeoaltimetry, lithology and/or provenance shifts and magmatic records (Wang et al., 2014a and references within). These methods suggest that the timing of the onset of uplift was at or shortly after initial collision at ~50-60 Ma (e.g. Yin et al., 2002; Clark et al., 2010; Qi et al., 2016; Bush et al., 2016) and continued into the Pliocene-Quaternary (e.g. Tapponnier et al., 2001).

The timing of Qilian Shan uplift is also linked with the debated pattern of Tibetan surface uplift after collision: progressive plateau growth, stepwise growth, or rapid regional uplift long after initial collision (summarised in Law and Allen, 2020). There is some thermochronology and other evidence for exhumation and deformation in the early Cenozoic in northern Tibet i.e. not long after the initial India-Eurasia collision. There is also increasing evidence for renewed exhumation in the Early Miocene or later (e.g. Zhu et al., 2006; Zheng et al., 2010; Lease et al., 2011; Zhang et al., 2012; Bush et al., 2016; Duvall et al., 2013; Zuza et al., 2016, Qi et al., 2016; Liu et al., 2017; Zheng et al., 2017; Pang et al., 2019). It is not clear whether these data collectively record deformation progressing northwards across the Qilian Shan, a more regional and synchronous deformation across the range, or

deformation and exhumation stepping outwards from the interior of the range to both the north and south, in a pattern that might be predicted if the range operated as a large-scale flower structure. No clear spatial pattern is clear in the recent summary of thermochronology data by Tong et al (2019), although the distinction seems clear between clusters of early (largely Eocene) and late Cenozoic (largely Miocene) exhumation ages. Yuan et al (2013) noted that, whatever the exact pattern of deformation and exhumation across the Qilian Shan, there are sufficient data to suggest growth initiated prior to the Pliocene.

The Qilian Shan consists of a series of WNW-ESE trending ridges, each ~700 km long and ~50 km wide, with an overall area of 250,000 km². The Qilian Shan is bounded by the Qaidam Basin to the south, the Hexi Corridor to the north and the Tarim Basin to the northwest (Figure 1). Peaks are over 5000 m and average elevation is 3500-4000 m. This compares to elevations of ~2750 m in the Qaidam Basin, and 900-1200 m in the Tarim Basin. Crustal thickness in the area is ~60-70 km, compared to ~55 km in the interior of the Qaidam Basin and 45-50 km in the Tarim Basin and Hexi Corridor areas, derived from the crustal P- and S-wave structure (Wang et al. 2013). The area is seismically active (Figure 2), with destructive historical earthquakes and earthquake-induced landsliding (Tang et al., 2012; Xu et al., 2010; Gaudemer et al., 1995).

Lower Palaeozoic and Proterozoic basement formed during accretion of several arcs and microcontinents to each other and the southwest margin of the North China Craton (Song et al., 2013; Zuza et al., 2018). These rocks were deformed and metamorphosed before the deposition of an Upper Palaeozoic cover sequence, which was then itself overlain by Mesozoic non-marine clastic rocks. Cenozoic alluvial, fluvial and lacustrine sediments have been deposited in intermontane basins (Horton et al., 2004).

The series of linear, Cenozoic thrust-fault-bounded ridges that collectively form the Qilian Shan accommodate most of the uplift in the area, and trend WNW-ESE (Figure 1; Tapponnier et al., 1990; Van der Woerd et al., 2001). Thrusts emerge at the base of the ranges, typically dipping >30^{o},

with the marginal thrusts at the northern range front dipping south, and thrusts at the southern margin dipping north (H. Zhang et al., 2017). Total GPS-derived convergence rates across the range are ~7-8 mm/yr (Wang et al., 2001). The frontal thrust in the region of the Shule River (Figure 4) accommodates 15 - 20 % of Qilian Shan shortening, as calculated from river terrace uplift (Yang et al., 2018). Oblique convergence across the range is partitioned into dip-slip (~6.7 mm/yr) and strike-slip (4.2 mm/yr) components (Allen et al., 2017).

Left-lateral strike-slip faulting occurs in the area, mainly on the Haiyuan Fault. The Haiyuan Fault slips at ~5 mm/yr in its centre, measured from GPS data (Allen et al. 2017) and 2.7-3 mm/yr at the left-stepping restraining bend to the north of Hala Lake (Figure 1), from ^{10}Be-^{26}Al cosmogenic nuclide dating (Li et al., 2017). Strike-slip faulting contributes to surface uplift via restraining bends and thrusting at the western tip of the Haiyuan Fault at the Sule Nan Shan (H. Zhang et al. 2017; Figure 1). The Altyn Tagh Fault marks the northwestern boundary of the Tibetan Plateau, with a length of over 1200 km and a slip rate that varies along its length, but is thought to be typically ˜9 mm/yr decreasing to ˜2 mm/yr at its east end (Figure 1; Shen et al., 2001; Yin et al., 2002; Zheng et al., 2013). Dextral faulting occurs, trending NNW-SSE, in the south east region of the Qilian Shan, near Qinghai Lake, with slip rates of ~1 mm/yr on the Elashan and Riyueshan faults (Yuan et al. 2011).

Large ($M_W \geq 7$) earthquakes occur in the north of the Qilian Shan, on strike-slip and thrust faults, but are scarce in the southern Qilian Shan (Xu et al., 2010). Thrust earthquakes occur at the lower elevation margins of the Qilian Shan, but rarely in the interior; thrust earthquake epicentres $M_W \geq$ ~5.3 are not seen above the regional 3500 m elevation contour (Allen et al., 2017; Figure 2). This indicates that active seismogenic thrusting is not occurring in the high elevation, central area, with non-seismic shortening building elevations above 3500 m. Strain is highest in the north of the Qilian Shan (Zuza et al., 2016).

The structure of the Qilian Shan contributes to our knowledge of the Tibetan Plateau formation. Geodetic data are consistent with the Qilian Shan deforming via a low angle (17^{o}) detachment thrust,

which dips to the south under the range (Allen et al., 2017). This thrust is modelled to have oblique slip below seismogenic depths (~26 ± 8 km), and slip is partitioned into separate strike-slip (Haiyuan Fault) and thrust faults in the shallow crust (Figure 1). Decreasing rock uplift rates from the Qilian Shan frontal thrusts to the south west are interpreted as a decrease in the angle of the frontal thrust as it flattens with depth and soles onto the detachment (Hetzel 2013). Yin et al (2008) emphasised the importance of a north-dipping detachment thrust under the Qilian Shan, which is emergent on the southern side of the range. Another suggested deformation mechanism is distributed shortening on crustal thrust faults across the Qilian Shan (England and Houseman, 1986). The Haiyuan Fault has been suggested to act as a root to a flower structure (Pang et al., 2019). Estimates of the magnitude of Cenozoic shortening across the Qilian Shan-Nan Shan thrust belt, compared to the strain distribution, indicate that the magnitude of shortening is produced by a combination of distributed shortening and minor southward underthrusting of Asian lithosphere (Zuza et al., 2016). Each shortening mechanism would show higher erosion in the hanging walls of thrust faults, and therefore higher HI, ksn and SR, however these different structures and shortening mechanisms would produce different spatial patterns of geomorphic indices in the Qilian Shan, therefore we study the entire range to ascertain which mechanism most closely matches our results. The underlying detachment thrust would lead to a relatively high relief landscape above the locked portion of the fault, because this part of the fault produces major earthquakes. These earthquakes in turn produce landslides and episodic rock uplift. In comparison, above the creeping portion of the thrust, uplift rates would be more constant, creating a lower relief landscape with high ZR values. Distributed shortening across a flower structure, or with southward underthrusting would produce greater HI, SR and k_{sn} in the north of the Qilian Shan, due to higher strain in this region.

1c Tectonic geomorphology in the Qilian Shan

High topographic relief of the Qilian Shan coincides spatially with the location of faults (Figure 1) and can be termed ‘structural relief’ (Liu-Zeng et al., 2008). Rivers draining the Qilian Shan, mainly

flow parallel to thrust faults, along topographic lows between the mountain ridges (Figure 4). Some rivers cross thrusts, especially at the southern and northern range fronts. The northern range front is steep with broad, northward draining, gently sloping alluvial fans with active channel braiding, and deeply incised channels (Tapponnier et al. 1990). In the eastern Qilian Shan rivers drain into the Yellow River (Huang He) which flows to its outlet in Bohai Bay (Wang et al. 1986). Rivers that drain the south of the Qilian Shan enter the internally-drained Qaidam Basin. The central region of the Qilian Shan is internally drained. Zhang et al., (2014) used cosmogenic nuclide dating and analysis of basin fill deposits to show that Qinghai Lake was cut off from the Yellow River external drainage between 0.5 and 1.2 Ma by the isostatic response to Yellow River excavation. Landslide scarps are common in the Qilian Shan, from modern and ancient tectonically-induced landslides (Tang et al., 2012; Xu et al., 2010).

Under pre-steady state, rock uplift outstrips erosion and in steady-state conditions rates of erosion or extension balance rock uplift over a long period (Burbank and Anderson, 2001). Pan et al. (2010) identify a linear relationship between local relief and catchment-scale decadal erosion rates, as estimated from sediment load records in the Qilian Shan. The northern Qilian Shan has been suggested to have reached topographic steady state (Hetzel, 2013) as erosion rates are similar to millennial throw rates (Hetzel et al., 2004) and long-term vertical slip rates of 0.4 – 0.6 mm/yr in the frontal thrusts of the Qilian Shan (Zheng et al., 2010), although more recent millennial vertical slip-rates of 0.9 ±1 mm/yr in the northern Qilian Shan (Yang et al., 2018) suggesting pre-steady state conditions. 20 km to the south west of the frontal thrust lower erosion rates (0.02 -0.25 mm/yr) have occurred for ˜10 Myr, suggesting much lower rock uplift rates have occurred in this area since the initiation of thrust faulting (Zheng et al., 2010). Su et al. (2019) use hypsometric curves and SA plots and suggest that the topographic evolution of the eastern Qilian Shan is in pre-steady state, where denudation will soon match with rock uplift from mountain building. In areas where erosion outpaces soil production rates, landscapes respond to erosion by bedrock landsliding (Montgomery, 2001). OSL and AMS ^{14}C Dating of strath terraces of the Xie River, eastern Qilian Shan shows the proximal fault of

the North Frontal Thrust system to have remained active as deformation propagated basinwards (Xiong et al., 2017).

Previous work on tectonic geomorphology of the Qilian Shan has provided insights into plateau formation processes and rock uplift variations and fault displacements. For example, high resolution topography has been used to calculate displacements on thrust and strike slip faults (Bi et al., 2018; the Heli Shan thrust fault, northern Qilian Shan). Wang et al., (2019) assessed the channel steepness and concavity variations across the major rivers of the northern and western Qilian Shan. Variations were attributed to rock uplift rather than precipitation or underlying lithology and they concluded that the channel steepness is greatest at the frontal thrusts of the Qilian Shan and decreases to the South and suggested that this is due to distributed crustal shortening in this area, concentrated on the thrust fault bounded ranges and underthrusting of Asian lithosphere (Wang et al., 2019), consistent with Zuza et al., (2016). Decadal erosion rates have been correlated with local topographic gradient and rock fracture density and rainstorm intensity for 11 drainage basins in the northern Qilian Shan (Pan et al., 2010; Wang et al., 2014). Rock uplift along the northern margin of the Qilian Shan is shown to be greater in the middle and western portions than the east, as calculated from channel steepness (Hu et al., 2010; Li et al., 2019) and catchment wide erosion rates (Palumbo et al., 2011). All of these studies were carried out in the northern Qilian Shan and therefore provide no means of testing for spatial variations in geomorphology across the Haiyuan, as are predicted by the model of change from locked to creeping deformation on the underlying detachment (Allen et al., 2017). H. Zhang et al., (2017) used river longitudinal profiles and geomorphic indices of topographic slope, local relief and channel steepness in the northern Qilian Shan to identify a plateau-like structure, with suggested relict erosional surfaces to the south of the Haiyuan Fault and intermontane aggradation forming the landscape to the north of the Haiyuan fault. They calculated one knickpoint for each of the 6 major rivers of the Qilian Shan (Figure 4), using the SRTM dataset and conventional methods. The knickpoints are close to active faults, and confirm the Qilian Shan to be in a transient state, but do not show a systematic pattern with elevation. The results were not considered in relation

to an underlying detachment. To build on these previous studies, we use a broader range of geomorphic indices, each providing complementary results and apply the techniques to the whole of the Qilian Shan, rather than localised areas.

We use digital topography from the 3 arc second (~90 m pixel size), Shuttle Radar Topography Mission (SRTM) (http://www2.jpl.nasa.gov/srtm/) to analyse Qilian Shan geomorphology at the regional scale. Sensitivity testing (Supplementary Figure 1) shows similar results for use of 30 m or 90 m data, therefore 90 m was used throughout for faster processing speed. Geomorphic indices hypsometric integral (HI), elevation-relief ratio (ZR), surface roughness (SR) and normalised channel steepness (k_{sn}) are analysed.

This work integrates geomorphic indices with recent structural and geodetic results in the Qilian Shan (Zheng et al., 2013; Zuza et al., 2016; Allen et al., 2017). The work aims to help to constrain the underlying structure of the Qilian Shan, which gives insights into the wider Tibetan Plateau formation, whilst also considering the relative roles of tectonics, precipitation and surface processes (Liu-Zheng et al., 2008) on the Qilian Shan formation. More broadly, the work shows the potential of these geomorphic indices to constrain fault locations and deep structure in other fold-and-thrust belts as (Gao et al., 2016; Nennewitz et al., 2018).

2 - Methods

2a - Hypsometric Integral (HI)

Hypsometry describes the distribution of elevation within an area (Pike and Wilson, 1971). The hypsometric integral (HI) is a method of differentiating between landscapes at different stages of landscape evolution (Strahler et al. 1952). HI is calculated as the integral of a hypsometric curve: a plot of normalised elevation against normalised drainage area for each drainage basin. Where surface uplift rate is greater than erosion within a catchment there is a greater range of elevation in the area,

giving a high HI. Therefore high HI values are typically found in areas of rapid uplift, although values can also be controlled by external factors, including rock type and precipitation.

HI (Figure 5) was calculated using TecDEM software (Shahzad and Gloaguen, 2011), for drainage basins. The rationale is that the boundaries of drainage basins may be controlled by tectonic and geological features, and are therefore natural boundaries between different uplift and river characteristics. Therefore, mapping HI by drainage basin avoids smoothing values over spatial boundaries such as faults, compared to other approaches such as moving windows (e.g. Obaid and Allen, 2019). HI was calculated for drainage basins of different orders, from 2nd Strahler order to 6th Strahler order (Supplementary Figure 2). The patterns of high and low HI regions are similar for each order, but 2nd order basins are shown here as these provide the most detail. Larger basins span fault traces and therefore obscure the changes in HI across fault boundaries. Basins were extracted from the SRTM data, based on a stream network defined with an upstream drainage area threshold of >1 km^2. This method produced an accurate stream pattern when compared to satellite imagery. Flat areas were removed after processing, to remove spurious results derived for lakes.

2b - Normalised Channel steepness (k_{sn})

Local channel slope for a steady-state river profile can be expressed as a power-law function of contributing drainage area e.g. Wobus et al., (2006):

$$S=k_s A^{-\Theta}$$

where S=Slope, k_s = steepness index, A=upstream drainage area and $\theta \approx$ concavity. The slope and area of the drainage basin is calculated. Channel steepness is calculated here based on a reference concavity to determine a normalised steepness index, k_{sn} (Wobus et al., 2006) allowing comparison of values between different basin sizes.

SRTM data was preprocessed and rivers extracted, using the TopoToolbox set of Matlab scripts (Schwanghart and Scherler, 2014). The TopoToolbox methodology is built upon the integral

method of river process analysis, after Perron and Royden (2013). Rivers were extracted with a minimum upslope area of >1 km² in order to remove areas of hillslope areas. Pixels of the area of lakes were then removed (Figure 6).

Both a calculated best-fit theta value and the most commonly used value of Θ=0.45 were used (Kirby et al., 2003) for comparison with previous studies. The averaged best-fit theta value was calculated by taking the best-fit values of theta for each of the major drainage basins of the Qilian Shan. The best-fit theta value is calculated as the gradient of a slope-area plot for each drainage basin as calculated by the TopoToolbox. The weighted average theta value was then calculated, weighted by catchment areas measured in ArcMap. The best-fit theta value was Θ=0.29. The results of these two analyses show the same pattern of k_{sn} on a map scale, but different values (see Supplementary Figure 3). The value of Θ=0.45 has been used in this paper as results can then be compared to other areas.

2c – ZR (Elevation-Relief Ratio)

The elevation-relief ratio (ZR ratio), calculated using the equation below, can be used to identify plateau-like areas: areas with high elevation and low relief (Formento-Truglio and Pazzaglia, 1998; Andronicos et al., 2007).

$$ZR = \frac{Mean\ Elevation\ (m)}{Maximum\ elevation\ (m) - minimum\ elevation\ (m)}$$

Second order stream basins were used, in line with the reasoning in section 2a. The mean elevation and range of elevation were calculated for each drainage basin in order to calculate the ZR (Figure 7). The ZR was also calculated by moving window, see Supplementary Figure 4.

2d – Surface Roughness: Standard Deviation of Slope

Surface roughness (SR) shows the variability of a topographic surface and is one of the most commonly used indices in geomorphology as it can be used to identify surface processes, uplift, feature type and material properties (e.g. Grohmann et al., 2010; Shahzad and Gloaguen, 2011;l Domínguez-González et al., 2015). There are multiple methods of characterising surface roughness, with Grohmann et al. (2010) concluding that the most appropriate measurement of the roughness of regional topography is the standard deviation of slope, as this correctly identified breaks of slope and smooth-sloping areas. SR was calculated for each second order drainage basin, calculating the standard deviation of the slope from 90 m resolution data, within each basin (Figure 8). SR was also calculated for a moving window, with the results showing a comparable pattern, see Supplementary Figure 5.

2e - Swath Profiles

Swath profiles show the variation of topography across a region. Spatial data is taken for a rectangular corridor of a given width, and across this width, minimum, maximum and mean values are extracted and condensed onto a single profile. Topographic swath profiles, of 30 km width, were created for 7 segments, trending NNE-SSW, perpendicular to the direction general WNW-ESE strike of the thrust faulting (Figure 9). Elevation data were extracted from the 90 m SRTM data with no smoothing. Maximum values represent the highest peaks, and minimum values, the valleys. The difference between the maximum and the minimum values is also shown, which represents the relief. Integration of the maximum-minimum difference gives the integrated relief (Obaid and Allen, 2019) which allows for comparison of relief across the range.

3 – Results

We split the Qilian Shan into 5 main parts in terms of morphology and geomorphic indices patterns. These are: the Central, internally drained region; the Northern region, with south-dipping thrust faults and rivers draining north into the Hexi Corridor; the Southern region, with north-dipping thrust faults and rivers draining south into the Qaidam Basin; the Western region, affected by the

Altyn Tagh Fault and the Eastern Qilian Shan which is drained by tributaries of the Yellow River (Figure 10). Four of these 5 areas are delineated by major drainage divides and therefore are natural boundaries between different conditions. The Western region of the Altyn Tagh Fault was considered separately, as this is a major structure which affects the landscape. Field photos of landscape variations in the Qilian Shan are shown in Supplementary Figure 6.

3a - Hypsometric Integral

Variations in HI values highlight the active faults of the area, particularly the active, WNW-ESE trending thrust faults (Figure 5). There are sharp boundaries along the fault traces, with abrupt changes from higher values in the hanging walls to lower values in the footwalls. In some areas a sharp change in values does not occur along a fault trace: in the Western region, high HI values occur on both sides of the Altyn Tagh Fault. In this study HI values range from 0 - 0.31, with values > 0.2 considered as high.

HI distributions show a distinct pattern of higher HI (> 0.2) in the north and east of the Qilian Shan than in the south and west. Values of HI > 0.15 are largely at or below 3500 m elevation. The overall pattern shows a boundary between the high and low values aligned with the Haiyuan Fault. There is also a pattern of high HI values across the margins of the mountain chain and low values in the central region, which is indicative of the plateau morphology.

The pattern of HI is strongly linked to the drainage pattern of the Qilian Shan. Low values of HI (< 0.1) occur in the central Qilian Shan, centred around the areas of internal drainage of Lake Hala and Lake Qinghai. Low values are also seen in the rivers draining to the south into the Qaidam Basin. Higher values (> 0.15) occur in the Eastern region, along the basins draining into the Datong and Huangshui rivers, which are tributaries of the Yellow River.

The 5 areas of the Qilian Shan discussed here were statistically analysed. The Kruskal-Wallis test (p value < 0.05) shows that there are significant differences between the HI values of the 5 areas.

Mann-Whitney U test analyses compared the data of the 10 combinations of areas, with results showing all areas to be distinct from each other ($p < 0.05$).

3b - Normalised Channel Steepness

K_{sn} values vary with climatic setting, rock strength and erosion/rock uplift (Kirby and Whipple, 2012). Underlying lithology and precipitation control are discussed in section 4.2 and are found to not be first order controls on $k_{sn,.}$ We therefore interpret our k_{sn} results with respect to changes in erosion and/or surface uplift.

The regions of highest k_{sn} are in the north and east of the Qilian Shan (Figure 6). Localised regions of high k_{sn} occur at major faults, as for the HI distributions. The k_{sn} values show a pattern of higher values ($k_{sn} > 50$) in the hanging wall of thrust faults. The width of the high k_{sn} regions varies, with wider regions (40 km wide where $k_{sn} > 50$) along the WNW-ESE trending thrust faults in the north, but 25 km wide in the south.

Rivers draining across active thrust faults in the northern Qilian Shan show some of the highest regional values of k_{sn} (> 100). Values are highest at the locations where the rivers cross the range fronts. The upper reaches of some of these rivers, such as the Beida River (Supplementary Figure 1, location shown in Figure 4), have lower k_{sn} values where they flow parallel to the ranges. High k_{sn} (> 50) values are also seen in the East Qilian Shan, representing rivers that flow into the Yellow River. The region of internal drainage has low values of k_{sn} (<50), indicating less steep rivers. The highest values of k_{sn} within the internally drained basins occurs in the rivers draining into Lake Qinghai, which is the largest of the three internal basins. High values of k_{sn} are found below the regional 3500 m elevation contour.

3c – ZR (Elevation Relief Ratio)

A high ZR ratio (in this study ZR > 6) indicates a low relief at higher elevation, mainly >3500 m, which is indicative of a plateau geomorphology. The Central Qilian Shan, around Hala Lake shows ZR above 6, showing plateau-like relief. There are low values (ZR < 4) on the northern and southern margins (Figure 7). Anonymously high values are also seen in very flat basins, such as the Qaidam Basin to the south of the Qilian Shan, simply due to their very low relief.

3d – Surface Roughness

The standard deviation of slope (Figure 8) shows a similar pattern to the HI values, with high values (SR >10) in the hanging walls of the thrust faults. The lowest values (<4) are seen in the lowlands surrounding the mountain chain and in the centre of the Qilian Shan, around Qinghai and Hala lakes. Surface roughness shows a less clear relationship with the drainage divides and regions of >3500 m elevation.

3e - Swath Profiles

The elevation profiles (Figure 9) show the plateau morphology of the interior of the Qilian Shan, with swaths 2-6 showing the clearest plateau morphology: shallower slopes in the south, a flatter area in the centre with maximum elevations of ~5500 m, and steeper slopes at the northern mountain front. There appears to be a sharper transition from the range front to the internally-drained plateau region in the north than the south. Swath 1 shows a similar trend, but with a steeper southern margin and a shallower northern margin. This difference may be due to the curvature of the mountain front, which in this region is not parallel to the swaths. Swath 7 shows high relief throughout. The relief curves of swaths 1-6, calculated as the difference between the maximum and minimum elevations, show an overall increase in relief from south to north.

4 – Discussion

4.1 Morphology of the Qilian Shan

The Northern region shows bands of high HI, k_{sn} and SR and low ZR values (HI >0.15, k_{sn} >100, SR >10, ZR <2). These bands are in the hanging wall of the thrust faults. This pattern suggests that the thrust faults are actively uplifting. It is unlikely changes are due to lithological contrasts (section 4.2). The rivers draining these regions are steepened by the rock uplift, forming deeply incised valleys. The plan-view width of these incised landscape regions in the hanging walls of each fault decrease to the south, as discussed in section 3.1. This may indicate a combination of lower uplift rates towards the central plateau and/or steeper dipping faults and/or a different duration of fault activity. In the west of this region, the Dang and Shule rivers (Figure 4) have been diverted to flow parallel to the thrust faults, and exit the mountain chains parallel to these faults, giving lower values of HI <0.15, k_{sn} <75, SR <10 and higher ZR values (ZR >6).

The Southern region shows the same pattern of geomorphic indices as the Northern region, with high values of HI, k_{sn} and SR and low ZR in the hanging walls of thrust faults. The width of these regions are narrower than the northern margin, at ~35 km compared with ~60 km. This may be due to lower topographic slopes in the south Qilian Shan compared to the north, or due to variation in rock uplift. If these changes are attributed to rock uplift, the results suggest that the Qilian Shan shows an asymmetric pattern of deformation, with a broader region of active uplift at the northern margin.

The Altyn Tagh Fault affects drainage patterns in this area. Rivers in the area are deflected left-laterally by the fault and the area is characterised by braided rivers and alluvial fans (Mériaux et al., 2005). The Altyn Tagh Fault region has values of HI >0.15, k_{sn} >75, SR >8, ZR <4 and Figure 5 shows that the second order basins are elongated perpendicular to the fault and parallel to the rivers that pass into the Tarim Basin to the north. The high HI values here occur where there are deeply incised gorges cut into alluvial fans, due to the differences in elevation between the fan surfaces and the active channels. We suggest that there may be a climatic control on the high HI values in this region, and that downcutting of the fan surfaces is a response to base level fall, itself produced by aridification of the Tarim Basin. The timescales are not constrained.

The central area, between the north and south sets of WNW-ESE trending thrust faults has the characteristics of a plateau landscape, with low relief (Figures 8, 9, Supplementary Figure 8), high elevation (Figure 9), high ZR (ZR > 6) Figure 7), low k_{sn} (< 50, Figure 6) and low HI (HI <0.1, Figure 5) and internal drainage. The geomorphic indices indicate a flatter landscape which is not being incised to the same extent as surrounding regions. This result is consistent with the work of Liu-Zeng et al. (2008), who used relief patterns to delineate the plateau-like landscape in the interior of the Qilian Shan.

The East region of the Qilian Shan drains into tributaries of the Yellow River (Figure 4), which is the only river in the area which reaches the sea. The South and Central areas are internally drained – rivers in the Central region drain into the lakes and rivers in the southern region into the Qaidam Basin, at ~2750 m elevation. The west and north fringes of the Qilian Shan drain further into the interior of Asia, to elevations of ~1400 m. The East region drains to the Bohai Sea. Swath profile 7 (Figure 9) shows that the morphology of the Eastern area varies from the plateau-like morphology of the central Qilian Shan. Instead, there is no high flat, central region and there is a large variation in each of the indices which simply represents the location of river channels, where the rivers incised deep valleys. This is attributed to the Datong and Huangshui rivers running parallel to the range, in contrast to the other major rivers of the Qilian Shan, particularly the Northern Qilian Shan, which flow orthogonal to the range, crossing the faults. The rivers are orthogonal to swath 7, therefore showing a different morphology in the swath profile (Figure 9 and Supplementary Figure 8). The area shows relatively high values of HI (>0.15), k_{sn} (>100), SR (>8) and low (ZR <6). This may be due to the relative ease of excavating the valleys parallel to the major thrust faults. Headward erosion due to base-level changes (Shi, 2019), and the larger, externally-drained, upstream area may also account for high HI and SR (Figure 10), but as there is no correlation between geomorphic indices and precipitation the higher values are not due to greater precipitation (Supplementary Figures 9, 10).

Drainage divides can be produced by tectonics, including both strike-slip and thrust faulting. The major basins are mostly defined by strike slip faulting: The left-lateral Altyn Tagh Fault, the North-East and North-Central by the left-lateral Haiyuan Fault, the Central-East by the right-lateral Riyueshan Fault and the Central-South by the right-lateral Elashan Fault (Figure 8). Strike-slip faulting often offsets and defeats rivers (Burbank and Anderson, 2001) and this process is crucial in plateau formation. The coincidence of drainage boundaries and strike slip faulting suggests that the faulting is aiding plateau formation in the Qilian Shan and therefore is a major control on the overall landscape of the Qilian Shan. Plateau formation will be in competition with externally drained rivers cutting back into the internally drained areas. The North-South and Central-East drainage boundaries (south of Qinghai Lake) are controlled by thrust fault location.

Integration of the relief of the profiles shows a variation in results (Figure 9) of 66 % (176 km² to 292 km² - a difference of 116 km²). The largest integrated relief (Profile 7) is in the east of the Qilian Shan, with the swath sampling the area drained by the Yellow River tributaries. Excluding this swath, the variation of swaths 1-6 is 36 %. Obaid and Allen (2019) found variations of < 25% across the Zagros, which they suggest to be a low value considering the variation in structure and climate across the range, and therefore the integrated relief value is more likely controlled by factors that are similar across the strike of the range, such as strain rate, overall shortening and elevation differences between plateau and foreland. The value of 36 % suggests that broadly similar factors may be controlling the relief in this area, apart from in the location of swath 7.

4.2 Precipitation, Lithology and Geomorphic Indices

Previous studies in other regions have shown that precipitation is positively correlated with erosion rates in areas with relatively low rates of tectonic rock uplift, and high precipitation would therefore produce higher values of HI and SR and low ZR and k_{sn} (Montgomery and Brandon, 2002; Henck et al., 2011). Annual precipitation (WorldClim version 2) for 1970-2000 for the Qilian Shan is shown in Figure 3. There is a precipitation gradient parallel to the Qilian Shan, with precipitation

decreasing from east to west. Precipitation is also higher in the northern margin of the Qilian Shan than the southern margin, which is likely to be due to higher elevations in the north, but may partially account for higher HI, k_{sn} and SR in the north. However, overall in the Qilian Shan, there is a very weak relationship between annual precipitation and HI, k_{sn} SR and ZR respectively (r^2 = 0.11, 0.06, 0.05, 0.14 respectively all p values < 0.05; see Supplementary Figure 9a) and between precipitation in July and the indices (r^2 = 0.14, 0.05, 0.02, 0.07, p values < 0.05; Supplementary Figure 9b) which is the wettest month and accounts for 24% of the annual precipitation. No east-west variation is observed in the HI, k_{sn} or SR or ZR, apart from in the Eastern region, with the higher HI, k_{sn} and SR and lower ZR values here attributed the range parallel rivers in this area (section 4.1). Figure 10b and Supplementary Figure 7, show an east-to-west decrease in precipitation but no east-to-west change in any of the indices. There is also poor correlation between the indices and storminess as calculated as the runoff coefficient of variation by Wang et al., (2014b) areas steeper than 20° for 11 basins in the northern Qilian Shan indices (r^2 = 0.27, 0.10, 0.11, 0.15, p values < 0.05). HI is more sensitive to storminess than the other indices. Decadal erosion is low in the Qilian Shan compared to other regions of active shortening such as the Himalayas (Li et al., 2014) and is weakly correlated to the geomorphic indices (Supplementary Figure 11; r^2 = 0.34, 0.39, 0.53, 0.35, p values < 0.05). Pan et al., (2010) found no relationship between decadal erosion rates and precipitation on a catchment scale in the northern Qilian Shan, although variables such as discharge and runoff may account for some of the variation in erosion rates, and may therefore account for variations in the geomorphic indices. We therefore conclude that precipitation variation and storminess do not control the geomorphic indices calculated in this study and are therefore not a first order control on landscape in the area. Decadal erosion rates, which are likely to be partially controlled by precipitation shows a stronger relationship with geomorphic indices. Su et al. (2017) also found no correlation between k_{sn} and precipitation in the Qinghai Nanshan (Figure 4), in the south of our area of study and therefore concluded that precipitation is not the main control on geomorphological evolution. Our finding that precipitation does not exert a major control on landscape despite a five-fold difference along the Qilian Shan

therefore seems to be robust, and in line with previous studies. This result is of interest as many studies in other regions conclude that precipitation is a major control on geomorphology (e.g. Ferrier et al., 2013; D'Arcy and Whittaker, 2014; Han et al., 2014). The key point of difference may be the relatively low rates of precipitation in the Qilian Shan, compared with regions in previous studies.

The underlying lithology of the area can also potentially influence landscape. Figure 11a shows the distributions of Precambrian basement and granite (Y. Zhang et al., 2017), in comparison to the pattern of HI. In terms of erodibility, these lithologies are the most resistant to erosion, compared to other lithologies in the area (Moosdorf et al., 2018). Basement and granite outcrops are coincident with a range of values of the geomorphic indices, and geomorphic index values overlying these lithologies are near identical to those for all other lithologies (Supplementary Figure 12). This suggests that lithology is not a major control on changes in HI and the other geomorphic indices. Changes in values across thrust faults (Section 4.1) are therefore attributed to changes in uplift rates and their consequences, rather than lithological changes. Comparison of underlying lithology and precipitation with channel steepness for major rivers in the northern Qilian Shan by Hu et al. (2010) also shows no relationship between them.

4.3 Underlying Structure and Geomorphic Indices

As precipitation and underlying lithology are not controlling the geomorphic index values, the results can be analysed in terms of tectonic control. Overall, the results of this study highlight active thrust faulting, with stepped increases in index values across the thrust faults. In general, thrust faults in the north of the Qilian Shan dip to the south and thrust faults in the south dip to the north. There is also a south-to-north increase in HI and k_{sn} coincident with the Haiyuan Fault. This increase is statistically significant (p value < 0.05) as calculated by a t-test on a moving area of 60 x 60 km, the extent of which is shown in Figure 12. A t-test was used as the data were shown by Q-Q plots to be normally distributed. 60 km was chosen, as this is the crustal thickness (Tian and Zhang, 2013) and a wide (larger than 60 km), straight section of the fault was selected to give a representative region.

This area was also selected as this is within the area where geodetic data was modelled by Allen et al., (2017). The best fitting lines, with the highest t-value, are shown to be within 2.5 km of the Haiyuan Fault in this area.

This distinct change in values of geomorphic indices from south to north across the Haiyuan Fault does not represent the location of maximum relief. The location of maximum relief for each of the 7 swath profiles (Figure 12a) shows the location the maximum value of the maximum-minus-minimum swath. These maximum relief values occur to the north of the Haiyuan Fault transition. The geomorphic index change is also coincident with the restraining bend of the Haiyuan Fault, but the change is seen to extend beyond this region, and therefore the restraining bend cannot account for the regional patter of geomorphic indices.

The abrupt change in geomorphic indices across the Haiyuan Fault may be due to drainage patterns, as drainage divides are reflective of boundary conditions. The drainage divide between the northern-draining and east-draining region is controlled by the strike-slip Haiyuan Fault. This drainage divide is therefore coincident with the change in geomorphic index values, and could be the cause of the change in geomorphic indices across the fault. However, we argue that as the drainage divide is between two externally-drained regions there should not be a large variation in index values. We would expect the largest change in values to be further to the south, between the Eastern region that drains into the Yellow River and the internally drained Central region, but there is no significant change in values across this boundary.

Uplift on inward-dipping thrust faults is consistent with the Qilian Shan having an overall flower structure at upper crustal levels (Yin et al., 2008 ; Pang et al., 2019), with wider regions of high HI, SR and k_{sn} in the north than the south possibly due to higher strain on the northern margin (Zuza et al., 2016). However, this model would not produce the observed change in values across the Haiyuan Fault and therefore does not fully explain the geomorphic signals seen at the regional scale.

This model is also not consistent with the locked-creeping transition identified by analysis of geodetic data in the area by Allen et al., (2017).

The patterns of the geomorphic indices are consistent with inward-dipping thrust faults, rooting onto a south-dipping detachment thrust (Meyer et al., 1998; Allen et al., 2017). The overall higher values of HI, k_{sn} and SR in the north of the Qilian Shan could represent higher uplift rates at the steepest portion of the detachment thrust, which is suggested to occur in this region (Hetzel 2013). However, due to the statistically significant change in HI and k_{sn} values across the Haiyuan Fault, calculated by the moving window t-test, we suggest that the increased HI and k_{sn} values to the north of the fault relate to the transition from the up-dip limit of creep on the underlying detachment thrust, as suggested by Allen et al. (2017) on the basis of elastic dislocation modelling of GPS data. They proposed that the left-lateral, strike-slip Haiyuan Fault marks the surface boundary of the transition from oblique creep below the seismogenic depth (~26 km) on a south-dipping detachment, to partitioned strike-slip and thrust faulting above i.e. from seismogenic faulting in the upper crust to ductile deformation below it. (Figure 13). This work constrains the geometry of the detachment, but not of the other faults in the area. The structure shown in Figure 13 is schematic, but is consistent with the geomorphic indices of this study.

Geodetic data was modelled by Allen et al (2017) from a wider region than that of the t-test (pale blue line, Figure 12), but sparse data meant that the analysis was not extended further to the east or west. A second t-test, over a 550 km extent of the Qilian Shan, of 30 km width, reveals the pattern of high values to the north of the black dashed line (Figure 12) and lower values to the south (p value < 0.05) to be continuous across the Qilian Shan. High values in this area partially correspond to the hanging wall of a thrust fault, but the pattern of high values to the north is not confined to this region. The geomorphic indices therefore suggest that the transition from locked to creeping deformation may extend across the area, not just in the region of the Haiyuan Fault. We suggest the change from locked to creeping can be said to be partially coincident with the Haiyuan Fault. The use

of geomorphic indices, which can be calculated across the whole range, is therefore used to infer a continuation of the structure predicted by the geodetic analysis, where GPS data was too sparse.

Assuming deformation on an underlying detachment, the Central portion of the Qilian Shan, where the statistically significant value changes are coincident with the Haiyuan Fault (HI from < 0.05 to > 0.1, k_{sn} from < 20 to > 75), is shown to be deforming remarkably simply under oblique convergence conditions. The deformation mechanism is more complicated to the west, where the change is to the north of the Haiyuan Fault, but a plateau morphology is still forming (Figure 9). This is likely to be due to internal drainage, with erosion on steep slopes and deposition within the basins creating a flatter landscape. The western margin is also deforming more complexly, due to strike-slip movement of the Altyn Tagh Fault deflecting structures and to some degree controlling the location and intensity of thrusting within the interior of the Qilian Shan (Meyer et al., 1998; Cheng et al., 2015). The historical earthquake record is also consistent with an underlying detachment. The locked-creeping transition is the likely southern limit for the largest earthquakes in the range (Allen et al., 2017) and therefore to the north of the Haiyuan Fault there is likely to be more seismic-induced landsliding, promoting high HI, SR and k_{sn} values and low ZR values. It is notable that the only *M* ~7 earthquakes recorded in the Qilian Shan are historic events along the northern margin of the range (Xu et al., 2010), or along the Haiyuan Fault (Gaudemer et al., 1995). Such major earthquakes may dominate the erosion budgets of the region, by analogy with other seismically active areas such as Taiwan (Dadson et al., 2003; Xu et al., 2010) although a weak positive correlation was found with erosion rate and accumulative seismic moment in the northern Qilian Shan (Wang et al., 2014b). This may be due to lower precipitation in the Qilian Shan meaning that landslide mass is not transported out of the basins as rapidly as in Taiwan, or because the 60 year time period used for the seismic moment did not include any earthquakes with $M_W \geq 7$. Above the creeping portion of the fault earthquakes and seismic-induced landsliding are less likely to occur, with more constant uplift, leading to flatter landscapes with higher ZR values.

The geomorphic indices are sensitive to drivers on a tectonic scale, showing the effect of the deep structure on the surface morphology. The results provide independent support for slip partitioning on an underlying detachment at depth, underneath the Haiyuan Fault (Allen et al., 2017; Bowman et al., 2003; Figure 13), while also confirming the development of lower relief, plateau-like landscape in the interior of the Qilian Shan (Liu-Zeng et al., 2008).

Application of the geomorphic indices in this study, combined with geodetic data analysis, to other fold-and-thrust belts can be used to assess whether the area is underlain by a detachment thrust e.g. Himalayas (Stevens and Avouac, 2015) or a set of individual thrust faults e.g. Zagros fold-and-thrust belt (Allen et al., 2013). We predict that the Himalaya and similar "detached" systems should be similar to the Qilian Shan, in terms of a geomorphic transition above the underlying change from creeping to locked thrust behaviour. More distributed systems, like the Zagros, should lack such a geomorphic transition.

5 - Conclusions

The east-west precipitation gradient of the Qilian Shan, which is orthogonal to the direction of shortening, provides an opportunity to assess the effect of precipitation on geomorphic indices in this area: precipitation is shown to not have a first order control on landscape. This result shows that a larger precipitation variation than the ~50 mm/yr to ~650 mm/yr variation along the Qilian Shan is needed to see an effect of precipitation on landscape, given the other parameters for this region such as strain rate, finite strain and landscape maturity (see Henck et al., 2011). Lithology variations are also not a first order control on landscape evolution.

We show that the pattern of high HI, k_{sn} and SR in the hanging walls of the inwardly-dipping thrust faults, and to the north of the left-lateral Haiyuan Fault is consistent with shortening on an underlying south-dipping detachment thrust, which changes behaviour from creeping to locked at the location of the Haiyuan Fault, as suggested by Allen et al., (2017). The geomorphic indices suggest this shortening mechanism to also be operating further to the west of the Haiyuan Fault , across the width

of the Qilian Shan, in an area with sparse GPS data, showing how the geomorphic indices can help our understanding of less accessible or less well monitored areas. The geomorphic indices used are sensitive to the underlying tectonic structure of the area and provide independent support for this structure, which was previously defined by modelling of geodetic data. The geomorphic changes across the Haiyuan fault and published geodetic analysis of Allen et al., (2017) do not support the idea that the Qilian Shan operates now as a flower structure (Pang et al., 2019), but does not rule out such a scenario operating at previous times.

These geomorphology approaches, and in particular the combination with geodetic modelling, could be used in future to assess how processes and structures vary among different fold-and-thrust belts and tectonic settings. In particular, we highlight the potential for differences between landscapes of fold-and-thrust belts where an underlying thrust detachment has been recognised, such as the Himalaya (Stevens and Avouac, 2015), and where this structural style may not apply, such as the Zagros (Allen et al., 2013).

Acknowledgements: This work was supported by the Natural Environment Research Council Iapetus Doctoral Training Partnership

6 - References

Allen, M.B., Saville, C., Blanc, E.J.-P., Talebian, M., Nissen, E., 2013. Orogenic plateau growth: expansion of the Turkish-Iranian Plateau across the Zagros fold-and-thrust belt. *Tectonics,* **32**, 171–190.

Allen, M.B., Walters, R.J., Song, S., Saville, C., De Paola, N., Ford, J., Hu, Z. and Sun, W., 2017. Partitioning of oblique convergence coupled to the fault locking behaviour of fold-and-thrust belts: Evidence from the Qilian Shan, northeastern Tibetan Plateau. *Tectonics*, **36**, 1679-1698.

Andronicos, C.L., Velasco, A.A. and Hurtado Jr, J.M., 2007. Large-scale deformation in the India-Asia collision constrained by earthquakes and topography. *Terra Nova*, ***19***, 105-119.

Bi, H., Zheng, W., Ge, W., Zhang, P., Zeng, J. and Yu, J., 2018. Constraining the distribution of vertical slip on the South Heli Shan Fault (northeastern Tibet) from high-resolution topographic data. *Journal of Geophysical Research: Solid Earth*, **123**, 2484-2501.

Bowman, D., King, G. and Tapponnier, P., 2003. Slip partitioning by elastoplastic propagation of oblique slip at depth. *Science*, ***300***, 1121-1123.

Burbank, D.W. and Anderson, R.S., 2001. *Tectonic geomorphology*. Blackwell Science.

Bush, M.A., Saylor, J.E., Horton, B.K. and Nie, J., 2016. Growth of the Qaidam Basin during Cenozoic exhumation in the northern Tibetan Plateau: Inferences from depositional patterns and multiproxy detrital provenance signatures. *Lithosphere*, **8**, 58-82.

Cheng, F., Jolivet, M., Dupont-Nivet, G. Wang, L. Yu, X. J. and Guo, Z. J., 2015. Lateral extrusion along the Altyn Tagh Fault, Qilian Shan (NE Tibet): Insight from a 3D crustal budget, Terra Nova, **27**, 416–425.

Cheng, F., Garzione, C.N., Mitra, G., Jolivet, M., Guo, Z., Lu, H., Li, X., Zhang, B., Zhang, C., Zhang, H. and Wang, L., 2019. The interplay between climate and tectonics during the upward and outward growth of the Qilian Shan orogenic wedge, northern Tibetan Plateau. *Earth-Science Reviews*, 198, 102945.

Clark, M.K., Farley, K.A., Zheng, D., Wang, Z. and Duvall, A.R., 2010. Early Cenozoic faulting of the northern Tibetan Plateau margin from apatite (U–Th)/He ages. *Earth and Planetary Science Letters*, **296**, 78-88.

Dadson, S.J., Hovius, N., Chen, H., Dade, W.B., Hsieh, M.L., Willett, S.D., Hu, J.C., Horng, M.J., Chen, M.C., Stark, C.P. and Lague, D., 2003. Links between erosion, runoff variability and seismicity in the Taiwan orogen. *Nature*, ***426****,* 733-736.

D'Arcy, M. and Whittaker, A.C., 2014. Geomorphic constraints on landscape sensitivity to climate in tectonically active areas. *Geomorphology*, **204**, 366-381.

Domínguez-González, L., Andreani, L., Stanek, K.P. and Gloaguen, R., 2015. Geomorpho-tectonic evolution of the Jamaican restraining bend. *Geomorphology*, **228**, 320-334.

Duvall, A., Clark, M.K., Kirby, E., Farley , K.A., Craddock, W.H., Li, C.Y. and Yuan, D.Y. 2013. Low-temperature thermochronometry along the Kunlun and Haiyuan Faults, NE Tibetan Plateau: Evidence for kinematic change during late-stage orogenesis. *Tectonics*, **32**, 1190-1211.

England, P. and Houseman, G., 1989. Extension during continental convergence, with application to the Tibetan Plateau. *Journal of Geophysical Research: Solid Earth*, **94**, 17561-17579.

England, P. and Houseman, G., 1986. Finite strain calculations of continental deformation: 2. Comparison with the India-Asia collision zone. *Journal of Geophysical Research: Solid Earth*, **91**, 3664-3676.

Elliott, J. R., R. J. Walters, P. C. England, J. A. Jackson, Z. Li, and B. Parsons (2010), Extension on the Tibetan Plateau: Recent normal faulting measured by InSAR and body wave seismology, *Geophys. J. Int.*, **183**, 503–535.

Ferrier, K.L., Huppert, K.L. and Perron, J.T., 2013. Climatic control of bedrock river incision. *Nature*, **496**, 206-209.

Fick, S.E. and Hijmans, R.J., 2017. WorldClim 2: new 1-km spatial resolution climate surfaces for global land areas. *International journal of climatology*, ***37***, 4302-4315.

Formento-Trigilio, M.L. and Pazzaglia, F.J., 1998. Tectonic geomorphology of the Sierra Nacimiento: Traditional and new techniques in assessing long-term landscape evolution in the southern Rocky Mountains. *The Journal of Geology*, **106**, 433-454.

Gao, M., Zeilinger, G., Xu, X., Wang, Q. and Hao, M., 2013. DEM and GIS analysis of geomorphic indices for evaluating recent uplift of the northeastern margin of the Tibetan Plateau, China. *Geomorphology*, **190**, 61-72.

Gao, M., Zeilinger, G., Xu, X., Tan, X., Wang, Q. and Hao, M., 2016. Active tectonics evaluation from geomorphic indices for the central and the southern Longmenshan range on the Eastern Tibetan Plateau, China. *Tectonics*, **35**, 1812-1826.

Gaudemer, Y., Tapponnier, P., Meyer, B., Peltzer, G., Shunmin, G., Zhitai, C., Huagung, D. and Cifuentes, I., 1995. Partitioning of crustal slip between linked, active faults in the eastern Qilian Shan, and evidence for a major seismic gap, the 'Tianzhu gap', on the western Haiyuan Fault, Gansu (China). *Geophysical Journal International*, **120**, 599-645.

Geng, H., Pan, B., Huang, B., Cao, B. and Gao, H., 2017. The spatial distribution of precipitation and topography in the Qilian Shan Mountains, northeastern Tibetan Plateau. *Geomorphology*, **297**, 43-54.

Grohmann, C.H., Smith, M.J. and Riccomini, C., 2010. Multiscale analysis of topographic surface roughness in the Midland Valley, Scotland. *IEEE Transactions on Geoscience and Remote Sensing***, 49**, 1200-1213.

Han, J., Gasparini, N.M. and Johnson, J.P., 2015. Measuring the imprint of orographic rainfall gradients on the morphology of steady-state numerical fluvial landscapes. *Earth Surface Processes and Landforms*, **40**, 1334-1350.

Henck, A.C., Huntington, K.W., Stone, J.O., Montgomery, D.R. and Hallet, B., 2011. Spatial controls on erosion in the Three Rivers Region, southeastern Tibet and southwestern China. *Earth and Planetary Science Letters*, **303**, 71-83.

Horton, B. K., G. Dupont-Nivet, J. Zhou, G. L. Waanders, R. F. Butler, and J. Wang (2004), Mesozoic-Cenozoic evolution of the Xining-Minhe and Dangchang basins, northeastern Tibetan Plateau: Magnetostratigraphic and biostratigraphic results. *J. Geophys. Res.*, **109**, (B04402).

Hetzel, R., Tao, M., Stokes, S., Niedermann, S., Ivy-Ochs, S., Gao, B., Strecker, M.R. and Kubik, P.W., 2004. Late Pleistocene/Holocene slip rate of the Zhangye thrust (Qilian Shan, China) and implications for the active growth of the northeastern Tibetan Plateau. *Tectonics*, **23**, (TC6006)

Hetzel, R., 2013. Active faulting, mountain growth, and erosion at the margins of the Tibetan Plateau constrained by in situ-produced cosmogenic nuclides. *Tectonophysics*, **582**, 1-24.

Hu, X., Pan, B., Kirby, E., Li, Q., Geng, H. and Chen, J., 2010. Spatial differences in rock uplift rates inferred from channel steepness indices along the northern flank of the Qilian Mountain, northeast Tibetan Plateau. *Chinese Science Bulletin*, **55**, 3205-3214.

Kapp, P. and DeCelles, P.G., 2019. Mesozoic–Cenozoic geological evolution of the Himalayan-Tibetan orogen and working tectonic hypotheses. *American Journal of Science*, **319**, 159-254.

Kirby, E. and Whipple, K., 2001. Quantifying differential rock-uplift rates via stream profile analysis. *Geology*, **29**, 415-418.

Kirby, E., Whipple, K.X., Tang, W. and Chen, Z., 2003. Distribution of active rock uplift along the eastern margin of the Tibetan Plateau: Inferences from bedrock channel longitudinal profiles. *Journal of Geophysical Research: Solid Earth*, **108**, (B42217).

Kirby, E. and Whipple, K.X., 2012. Expression of active tectonics in erosional landscapes. *Journal of Structural Geology*, **44**, 54-75.

Lacombe, O. and Bellahsen, N., 2016. Thick-skinned tectonics and basement-involved fold–thrust belts: insights from selected Cenozoic orogens. *Geological Magazine*, **153**, 763-810.

Law, R. and Allen, M.B., 2020. Diachronous Tibetan Plateau landscape evolution derived from lava field geomorphology. *Geology,* **48**, 263-267.

Lease, R., Burbank, D.W., Clark, M.K., Farley, K.A., Zheng, D.W. and Zhang, H.P., 2011. Middle Miocene reorganization of deformation along the northeastern Tibetan Plateau. *Geology,* **39***,* 359–362.

Li, Q., Pan, B., Gao, H., Wen, Z. and Hu, X., 2019. Differential rock uplift along the northeastern margin of the Tibetan Plateau inferred from bedrock channel longitudinal profiles. *Journal of Asian Earth Sciences*, **169**, 182-198.

Li, Y., Shan, X., Qu, C., Zhang, Y., Song, X., Jiang, Y., Zhang, G., Nocquet, J.M., Gong, W., Gan, W. and Wang, C., 2017. Elastic block and strain modeling of GPS data around the Haiyuan-Liupanshan fault, northeastern Tibetan Plateau. *Journal of Asian Earth Sciences*, **150**, 87-97.

Li, Y., Li, D., Liu, G., Harbor, J., Caffee, M. and Stroeven, A.P., 2014. Patterns of landscape evolution on the central and northern Tibetan Plateau investigated using in-situ produced 10Be concentrations from river sediments. *Earth and Planetary Science Letters*, **398**, 77-89.

Liang, S., Gan, W., Shen, C., Xiao, G., Liu, J., Chen, W., Ding, X. and Zhou, D., 2013. Three-dimensional velocity field of present-day crustal motion of the Tibetan Plateau derived from GPS measurements. *Journal of Geophysical Research: Solid Earth*, **118**, 5722-5732.

Liu, R., Allen, M.B., Zhang, Q., Du, W., Cheng, X., Holdsworth, R.E. and Guo, Z., 2017. Basement controls on deformation during oblique convergence: Transpressive structures in the western Qaidam Basin, northern Tibetan Plateau. *Lithosphere*, **9**, 583-594.

Liu-Zeng, J., Tapponnier, P., Gaudemer, Y. and Ding, L., 2008. Quantifying landscape differences across the Tibetan plateau: Implications for topographic relief evolution. *Journal of Geophysical Research: Earth Surface*, **113,** (FO4018).

Mériaux, A.S., Tapponnier, P., Ryerson, F.J., Xiwei, X., King, G., Van der Woerd, J., Finkel, R.C., Haibing, L., Caffee, M.W., Zhiqin, X. and Wenbin, C., 2005. The Aksay segment of the northern Altyn Tagh fault: Tectonic geomorphology, landscape evolution, and Holocene slip rate. *Journal of Geophysical Research: Solid Earth*, ***110*** (B4).

Meyer, B., P. Tapponnier, L. Bourjot, F. Metivier, Y. Gaudemer, G. Peltzer, G. Shunmin, and C. Zhitai , 1998, Crustal thickening in Gansu-Qinghai, lithospheric mantle subduction, and oblique, strike-slip controlled growth of the Tibet plateau, *Geophys. J. Int.*, **135**, 1–47.

Molnar, P., and H. Lyon-caen (1989), Fault plane solutions of earthquakes and active tectonics of the Tibetan Plateau and its margins, *Geophys. J. Int.*, **99**, 123–153.

Montgomery, D.R., 2001. Slope distributions, threshold hillslopes, and steady-state topography. *American Journal of science*, **301**, 432-454.

Montgomery, D.R. and Brandon, M.T., 2002. Topographic controls on erosion rates in tectonically active mountain ranges. *Earth and Planetary Science Letters*, **201**, 481-489.

Moosdorf, N., Cohen, S. and von Hagke, C., 2018. A global erodibility index to represent sediment production potential of different rock types. *Applied geography*, **101**, 36-44.

Nennewitz, M., Thiede, R.C. and Bookhagen, B., 2018. Fault activity, tectonic segmentation, and deformation pattern of the western Himalaya on Ma timescales inferred from landscape morphology. *Lithosphere*, **10**, 632-640.

Obaid, A.K. and Allen, M.B., 2019. Landscape expressions of tectonics in the Zagros fold-and-thrust belt. *Tectonophysics*, **766**, 20-30.

Palumbo, L., Hetzel, R., Tao, M. and Li, X., 2011. Catchment-wide denudation rates at the margin of NE Tibet from in situ-produced cosmogenic 10Be. *Terra Nova*, **23**, 42-48.

Pan, B.T., Geng, H.P., Hu, X.F., Sun, R.H. and Wang, C., 2010. The topographic controls on the decadal-scale erosion rates in Qilian Shan Mountains, NW China. *Earth and Planetary Science Letters*, **292**, 148-157.

Pang, J., Yu, J., Zheng, D., Wang, W., Ma, Y. and Wang, Y., 2019. Neogene expansion of the Qilian Shan, north Tibet: Implications for the dynamic evolution of the Tibetan Plateau. *Tectonics*, **38**, 1018-1032.

Perron, J.T. and Royden, L., 2013. An integral approach to bedrock river profile analysis. *Earth Surface Processes and Landforms*, **38**, 570-576.

Pike, R.J. and Wilson, S.E., 1971. Elevation-relief ratio, hypsometric integral, and geomorphic area-altitude analysis. *Geological Society of America Bulletin*, **82**, 1079-1084.

Poblet, J. and Lisle, R.J., 2011. Kinematic evolution and structural styles of fold-and-thrust belts. *Geological Society, London, Special Publications*, **349**, 1-24.

Qi, B., Hu, D., Yang, X., Zhang, Y., Tan, C., Zhang, P. and Feng, C., 2016. Apatite fission track evidence for the Cretaceous–Cenozoic cooling history of the Qilian Shan (NW China) and for stepwise northeastward growth of the northeastern Tibetan Plateau since early Eocene. *Journal of Asian Earth Sciences*, **124**, 28-41.

Royden, L.H., Burchfiel, B.C. and van der Hilst, R.D., 2008. The geological evolution of the Tibetan Plateau. *Science*, **321**, 1054-1058.

Schwanghart, W. and Scherler, D., 2014. TopoToolbox 2–MATLAB-based software for topographic analysis and modeling in Earth surface sciences. *Earth Surface Dynamics*, **2**, 1-7.

Shahzad, F. and Gloaguen, R., 2011. TecDEM: A MATLAB based toolbox for tectonic geomorphology, Part 1: Drainage network preprocessing and stream profile analysis. *Computers & Geosciences*, **37**, 250-260.

Shen, Z.K., Wang, M., Li, Y., Jackson, D.D., Yin, A., Dong, D. and Fang, P., 2001. Crustal deformation along the Altyn Tagh fault system, western China, from GPS. *Journal of Geophysical Research: Solid Earth*, **106**, 30607-30621.

Shi, C., 2019. Ages and magnitudes of base level fall and valley downcutting in ten tributaries (the Ten Kongduis) of the upper Yellow River, China. *Geomorphology*, **325**, 29-39.

Song, S., Y. Niu, L. Su, and X. Xia 2013, Tectonics of the North Qilian orogen, NW China, *Gondwana Res*earch, **23**, 1378–1401.

Stevens, V.L. and Avouac, J.P., 2015. Interseismic coupling on the main Himalayan thrust. *Geophysical Research Letters*, **42**, 5828-5837.

Strahler, A.N., 1952. Hypsometric (area-altitude) analysis of erosional topography. *Geological Society of America Bulletin*, **63**, 1117-1142.

Su, Q., Xie, H., Yuan, D.Y. and Zhang, H.P., 2017. Along-strike topographic variation of Qinghai Nanshan and its significance for landscape evolution in the northeastern Tibetan Plateau. *Journal of Asian Earth Sciences*, **147**, 226-239.

Su, Q., Yuan, D., Zhang, H., Manopkawee, P., Zhan, Y., Zhang, P. and Xie, H., 2019. Geomorphic evidence for northeastward expansion of the eastern Qilian Shan, northeastern Tibetan Plateau. *Journal of Asian Earth Sciences*, **177**, 314-323.

Tang, C., van Asch, T.W., Chang, M., Chen, G.Q., Zhao, X.H. and Huang, X.C., 2012. Catastrophic debris flows on 13 August 2010 in the Qingping area, southwestern China: the combined effects of a strong earthquake and subsequent rainstorms. *Geomorphology*, **139**, 559-576.

Tapponnier, P., Meyer, B., Avouac, J.P., Peltzer, G., Gaudemer, Y., Shunmin, G., Hongfa, X., Kelun, Y., Zhitai, C., Shuahua, C. and Huagang, D., 1990. Active thrusting and folding in the Qilian Shan, and decoupling between upper crust and mantle in northeastern Tibet. *Earth and Planetary Science Letters*, **97**, 382-403.

Tapponnier, P., Zhiqin, X., Roger, F., Meyer, B., Arnaud, N., Wittlinger, G. and Jingsui, Y., 2001. Oblique stepwise rise and growth of the Tibet Plateau. *Science*, **294**, 1671-1677.

Tejero, R., González-Casado, J.M., Gómez-Ortiz, D. and Sánchez-Serrano, F., 2006. Insights into the “tectonic topography” of the present-day landscape of the central Iberian Peninsula (Spain). *Geomorphology*, **76**, 280-294.

Tian, X. and Zhang, Z., 2013. Bulk crustal properties in NE Tibet and their implications for deformation model. *Gondwana Research*, **24**, 548-559.

Tong, K., Li, Z.W., Zhu, L., Tao, G., Zhang, Y.X., Yang, W.G. and Zhang, J.L., 2019. Fold-and-thrust deformation of the hinterland of Qilian Shan, northeastern Tibetan Plateau since Mesozoic with implications for the plateau growth. *Journal of Asian Earth Sciences,* 104131.

Van Der Woerd, J., Xu, X., Li, H., Tapponnier, P., Meyer, B., Ryerson, F.J., Meriaux, A.S. and Xu, Z., 2001. Rapid active thrusting along the northwestern range front of the Tanghe Nan Shan (western Gansu, China). *Journal of Geophysical Research: Solid Earth*, **106**, 30475-30504.

Wang, Y., Ren, M.E. and Zhu, D., 1986. Sediment supply to the continental shelf by the major rivers of China. *Journal of the Geological Society*, **143**, 935-944.

Wang, Q., Zhang, P.Z., Freymueller, J.T., Bilham, R., Larson, K.M., Lai, X.A., You, X., Niu, Z., Wu, J., Li, Y. and Liu, J., 2001. Present-day crustal deformation in China constrained by global positioning system measurements. *Science*, **294**, 574-577.

Wang, Y., Mooney, W.D., Yuan, X. and Okaya, N., 2013. Crustal structure of the northeastern Tibetan Plateau from the southern Tarim Basin to the Sichuan Basin, China. *Tectonophysics*, **584**, 191-208.

Wang, C., Dai, J., Zhao, X., Li, Y., Graham, S.A., He, D., Ran, B. and Meng, J., 2014a. Outward-growth of the Tibetan Plateau during the Cenozoic: A review. *Tectonophysics*, **621**, 1-43.

Wang, Y., Zhang, H., Zheng, D., Wenjun, Zheng, W., Zhang, Z., Wang, W. and Yu, J., 2014b. Controls on decadal erosion rates in Qilian Shan: Re-evaluation and new insights into landscape evolution in north-east Tibet. *Geomorphology*, **223**, 117-128.

Wang, Y., Zheng, D., Zhang, H., Li, C., Xiao, L., Li, Y. and Hao, Y., 2019. The distribution of active rock uplift in the interior of the western Qilian Shan, NE Tibetan Plateau: Inference from bedrock channel profiles. *Tectonophysics*, **759**, 15-29.

Wobus, C., Whipple, K.X., Kirby, E., Snyder, N., Johnson, J., Spyropolou, K., Crosby, B., Sheehan, D. and Willett, S.D., 2006. Tectonics from topography: Procedures, promise, and pitfalls. *Special papers-geological society of America*, **398**, 55.

Xu, X., Yeats, R.S. and Yu, G., 2010. Five short historical earthquake surface ruptures near the Silk Road, Gansu Province, China. *Bulletin of the Seismological Society of America*, **100**, 541-561.

Xiong, J., Li, Y., Zhong, Y., Lu, H., Lei, J., Xin, W., Wang, L., Hu, X. and Zhang, P., 2017. Latest Pleistocene to Holocene thrusting recorded by a flight of strath terraces in the eastern Qilian Shan, NE Tibetan Plateau. *Tectonics*, **36**, 2973-2986.

Yang, H., Yang, X., Huang, X., Li, A., Huang, W. and Zhang, L., 2018. New constraints on slip rates of the Fodongmiao-Hongyazi fault in the Northern Qilian Shan, NE Tibet, from the 10Be exposure dating of offset terraces. *Journal of Asian Earth Sciences*, **151**, 131-147.

Yin, A., Rumelhart, P.E., Butler, R., Cowgill, E., Harrison, T.M., Foster, D.A., Ingersoll, R.V., Qing, Z., Xian-Qiang, Z., Xiao-Feng, W. and Hanson, A., 2002. Tectonic history of the Altyn Tagh fault system in northern Tibet inferred from Cenozoic sedimentation. *Geological Society of America Bulletin*, **114**, 1257-1295.

Yin, A., Dang, Y.Q., Wang, L.C., Jiang, W.M., Zhou, S.P., Chen, X.H., Gehrels, G.E. and McRivette, M.W., 2008. Cenozoic tectonic evolution of Qaidam basin and its surrounding regions (Part 1): The southern Qilian Shan-Nan Shan thrust belt and northern Qaidam basin. *Geological Society of America Bulletin*, **120**, 813-846.

Yuan, D.Y., Champagnac, J.D., Ge, W.P., Molnar, P., Zhang, P.Z., Zheng, W.J., Zhang, H.P. and Liu, X.W., 2011. Late Quaternary right-lateral slip rates of faults adjacent to the lake Qinghai, northeastern margin of the Tibetan Plateau. *Bulletin*, **123**, 2016-2030.

Yuan, D.Y., Ge, W.P., Chen, Z.W., Li, C.Y., Wang, Z.C., Zhang, H.P., Zhang, P.Z., Zheng, D.W., Zheng, W.J., Craddock, W.H. and Dayem, K.E., 2013. The growth of northeastern Tibet and its relevance to large-scale continental geodynamics: A review of recent studies. *Tectonics*, **32**, 1358-1370.

Zhang, H.P., Craddock, W.H., Lease, R.O., Wang, W.T., Yuan, D.Y., Zhang, P.Z., Molnar, P., Zheng, D.W. and Zheng, W.J., 2012. Magnetostratigraphy of the Neogene Chaka basin and its implications for mountain building processes in the north-eastern Tibetan Plateau. *Basin Research,* **24**, 31-50.

Zhang, H., Zhang, P., Champagnac, J.D., Molnar, P., Anderson, R.S., Kirby, E., Craddock, W.H. and Liu, S., 2014. Pleistocene drainage reorganization driven by the isostatic response to deep incision into the northeastern Tibetan Plateau. *Geology*, **42**, 303-306.

Zhang, H., Zhang, P., Prush, V., Zheng, D., Zheng, W., Wang, W., Liu, C. and Ren, Z., 2017. Tectonic geomorphology of the Qilian Shan in the northeastern Tibetan Plateau: Insights into the plateau formation processes. *Tectonophysics*, **706**, 103-115.

Zhang, Y., Song, S., Yang, L., Su, L., Niu, Y., Allen, M.B. and Xu, X., 2017. Basalts and picrites from a plume-type ophiolite in the South Qilian Accretionary Belt, Qilian Orogen: Accretion of a Cambrian Oceanic Plateau?. *Lithos*, **278**, 97-110.

Zheng, D., Clark, M.K., Zhang, P., Zheng, W. and Farley, K.A., 2010. Erosion, fault initiation and topographic growth of the North Qilian Shan (northern Tibetan Plateau). *Geosphere*, **6**, 937-941.

Zheng, W. J., P. Z. Zhang, W. G. He, D. Y. Yuan, Y. X. Shao, D. W. Zheng, W. P. Ge, and W. Min 2013. Transformation of displacement between strike-slip and crustal shortening in the northern margin of the Tibetan Plateau: Evidence from decadal GPS measurements and late Quaternary slip rates on faults, *Tectonophysics*, **584**, 267–280.

Zheng, D., Wang, W., Wan, J., Yuan, D., Liu, C., Zheng, W., Zhang, H., Pang, J. and Zhang, P., 2017. Progressive northward growth of the northern Qilian Shan–Hexi Corridor (northeastern Tibet) during the Cenozoic. *Lithosphere*, **9**, 408-416.

Zhu, L., Wang, C., Zheng, H., Xiang, F., Yi, H. and Liu, D., 2006. Tectonic and sedimentary evolution of basins in the northeast of Qinghai-Tibet Plateau and their implication for the northward growth of the Plateau. *Palaeogeography, Palaeoclimatology, Palaeoecology*, **241**, 49-60.

Zuza, A.V., Cheng, X. and Yin, A., 2016. Testing models of Tibetan Plateau formation with Cenozoic shortening estimates across the Qilian Shan–Nan Shan thrust belt. *Geosphere*, **12**, 501-532.

Zuza, A.V., Wu, C., Reith, R.C., Yin, A., Li, J., Zhang, J., Zhang, Y., Wu, L. and Liu, W., 2018. Tectonic evolution of the Qilian Shan: An early Paleozoic orogen reactivated in the Cenozoic. *GSA Bulletin*, **130**, 881-925.

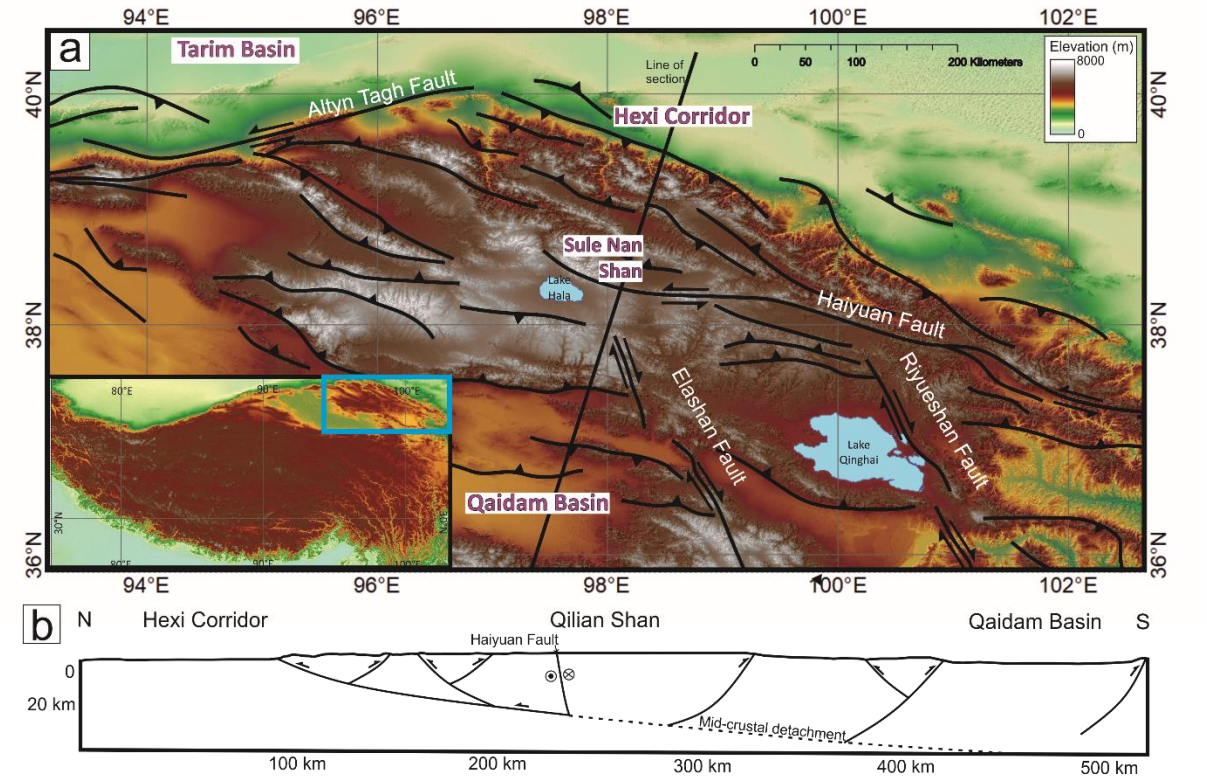

Figure 1.a. The regional structure and topography (SRTM) of the Qilian Shan and b. cross section of Qilian Shan. Thrust faults mainly strike WNW-ESE (Allen et al., 2017). Major strike-slip faults are labelled. Inset shows the location of the Qilian Shan, at the North East of the Tibetan Plateau.

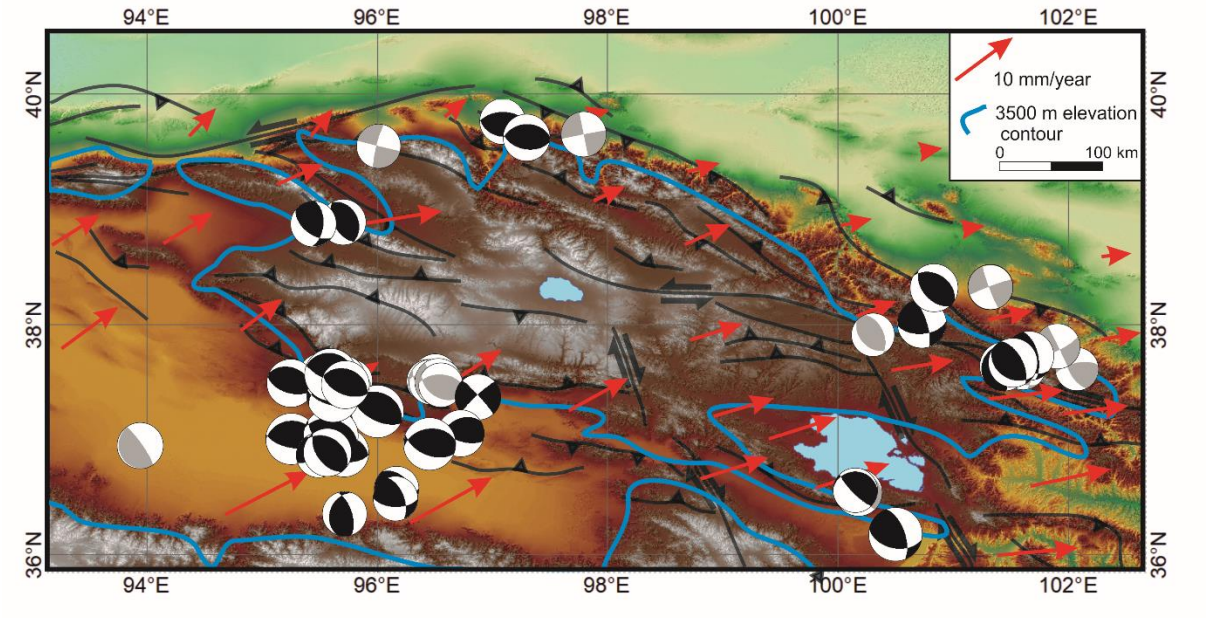

Figure 2. Seismicity and GPS velocities of the Qilian Shan. The black focal mechanisms are from body wave modelling (Molnar and Lyon-caen, 1989; Elliott et al., 2010) or the Global CMT catalogue where *M* >5.3 and there is >70% double couple (data to 2016). The grey focal mechanisms are from the Global CMT catalogue where *M* <5.3 and/or there is <70% double couple. Epicentres are clustered at and below the regional 3500 m contour line. GPS velocities are shown with respect to stable Eurasia, taken from Liang et al. (2013) and are oblique to the general WNW-ESE trend of the thrust faults.

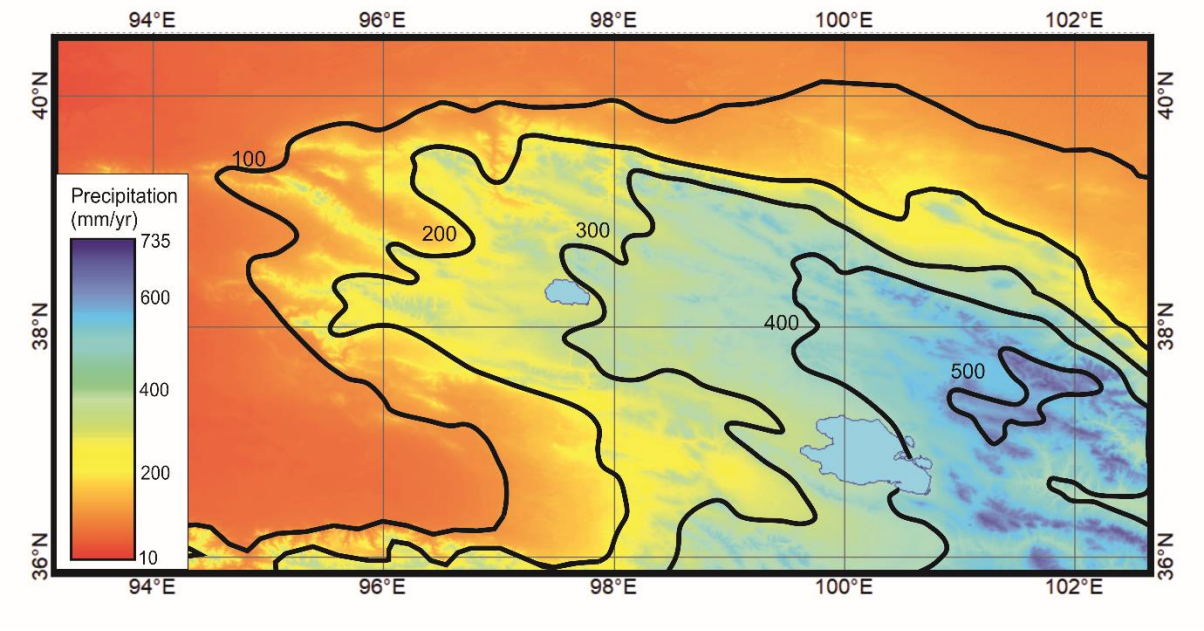

Figure 3. Mean annual precipitation (mm) for the study area from the years 1970-2000. Data from WorldClim, version 2 (Fick and Hijmans, 2017) shown overlain by smoothed contours. Precipitation generally decreases East (> 500 mm) to West (< 100 mm), across the Qilian Shan.

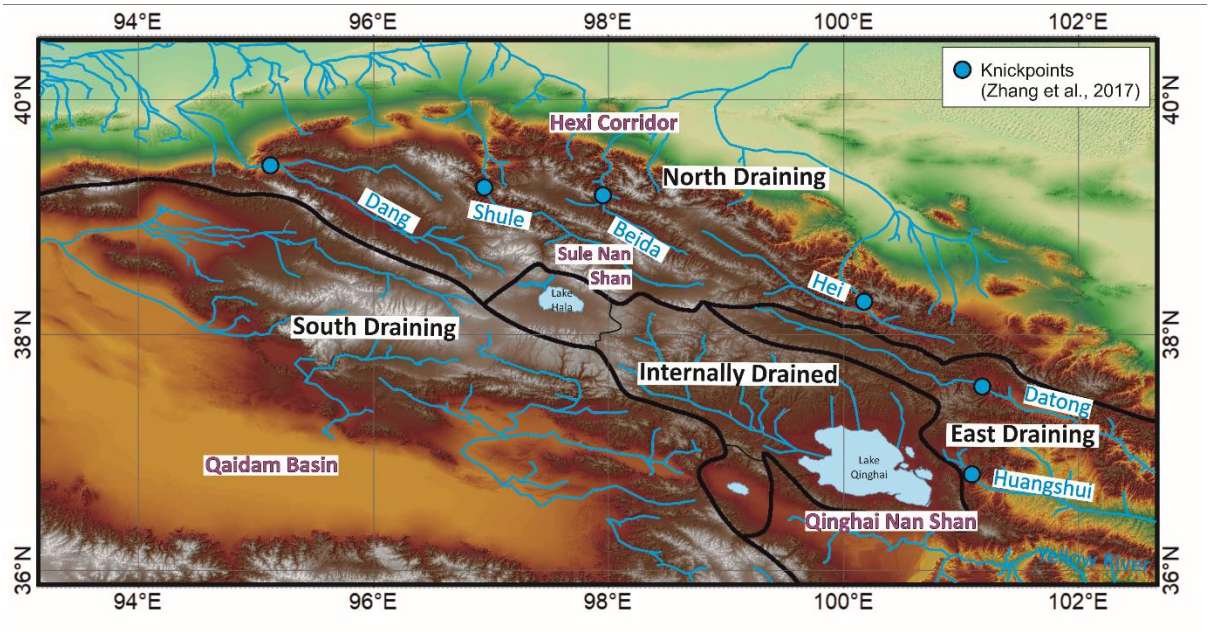

Figure 4. Major drainage divides and rivers of the Qilian Shan, extracted from SRTM data using the D8 algorithm. The major rivers, used in Figure 10 are labelled. These rivers are broadly divided into North Draining, East Draining, South Draining and Internally Drained rivers; divides are shown in black. Locations of knickpoints from Zhang et al., 2017 are shown.

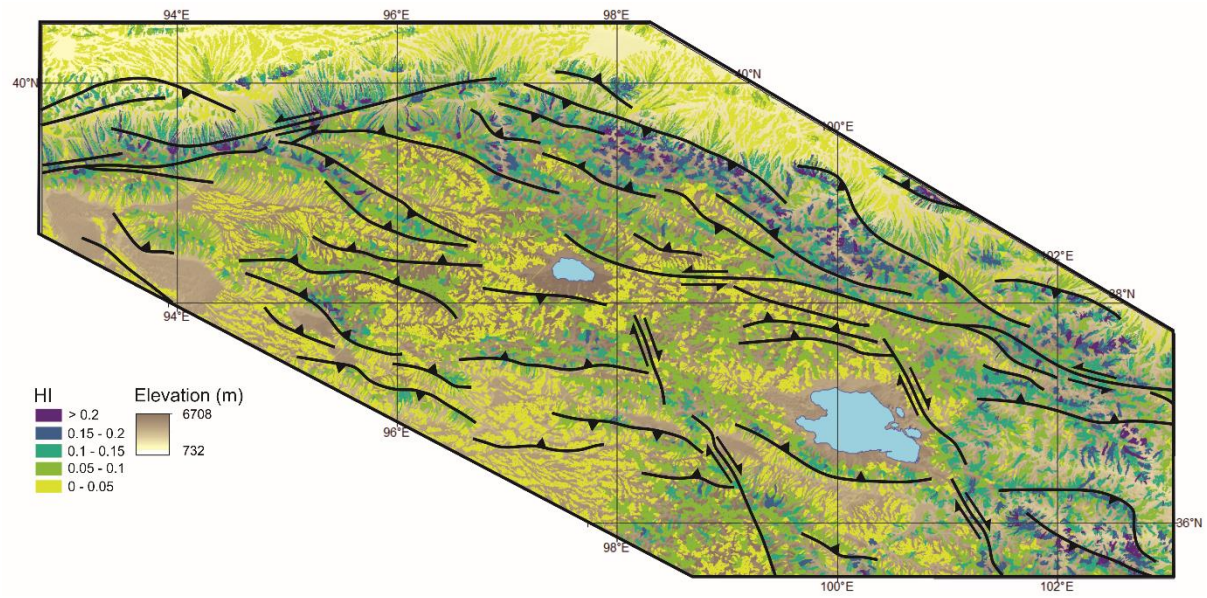

Figure 5. HI (Mean: 0.06; Maximum; 0.32 Standard Deviation: 0.04) for second Strahler order drainage basins, with fault traces shown. High HI (> 0.2) indicates landscapes with high rock and surface uplift and low HI (> 0.05) flatter landscapes. HI is sensitive to active faulting in the area, with high HI in the hangingwalls of thrust faults and along the Altyn Tagh Fault. HI values are higher in the North and East of the region, with a distinct increase in HI from south to north across the Haiyuan Fault.

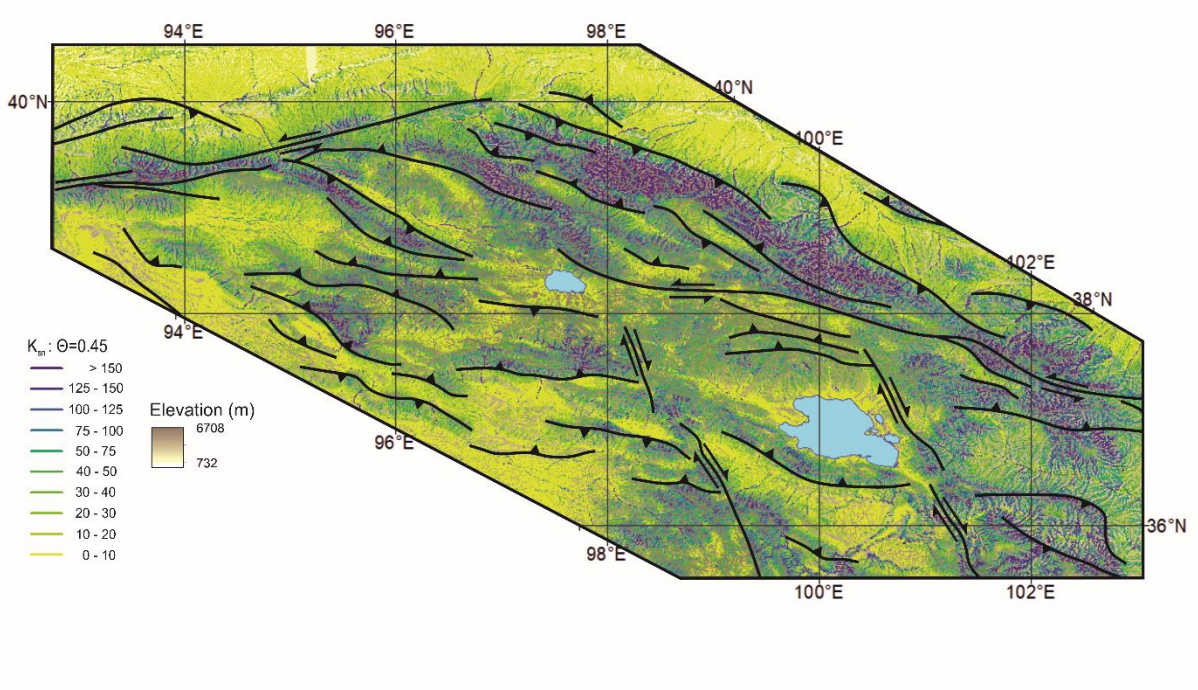

Figure 6. K_{sn} (Mean: 56; Maximum; 670 Standard Deviation: 83) of streams across the region, calculated with a reference concavity of Θ=0.45. Fault traces are also shown. High k_{sn} values (>75) occur in the north and south of the region, again with high values in the hangingwalls of active thrust faults.

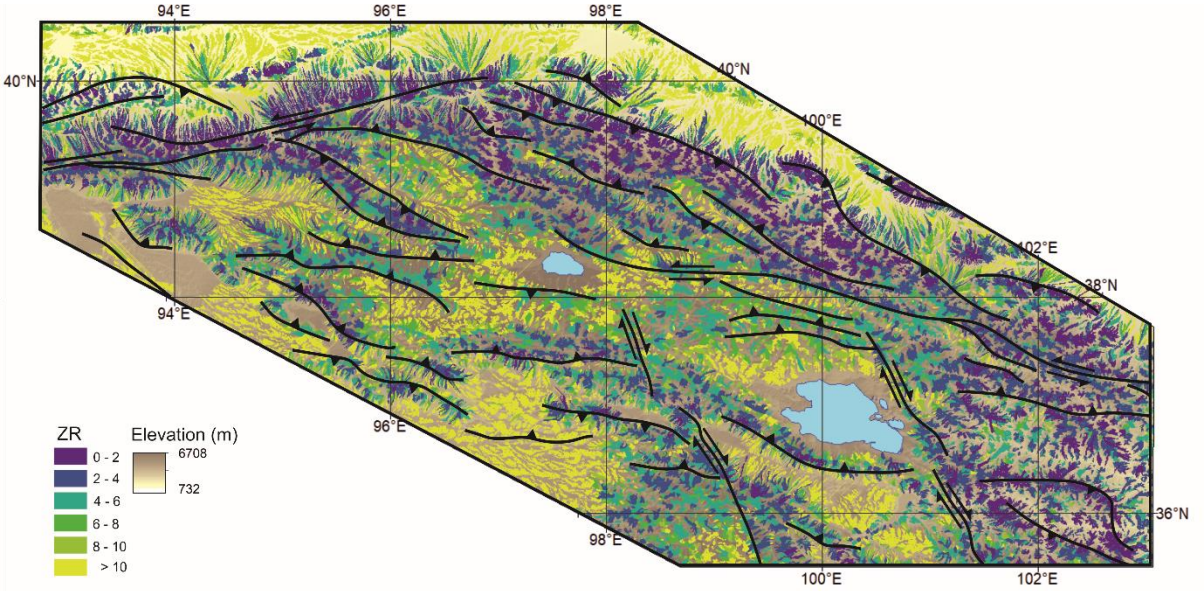

Figure 7. ZR (Mean: 19; Maximum; 351 Standard Deviation: 42) calculated for second Strahler order basins, shown with the faults of the area. High ZR (> 6) values are created by a combination of high elevation and low relief. The highest values occur in the flat basins surrounding the Qilian Shan, due to their low relief. High values also occur in the central region of the Qilian Shan, surrounding the lakes, showing these areas have a plateau-like morphology. Low ZR values (< 2) show low elevation and/or high relief. These areas are again in the north and east of the region, and in the hangingwalls of thrust faults.

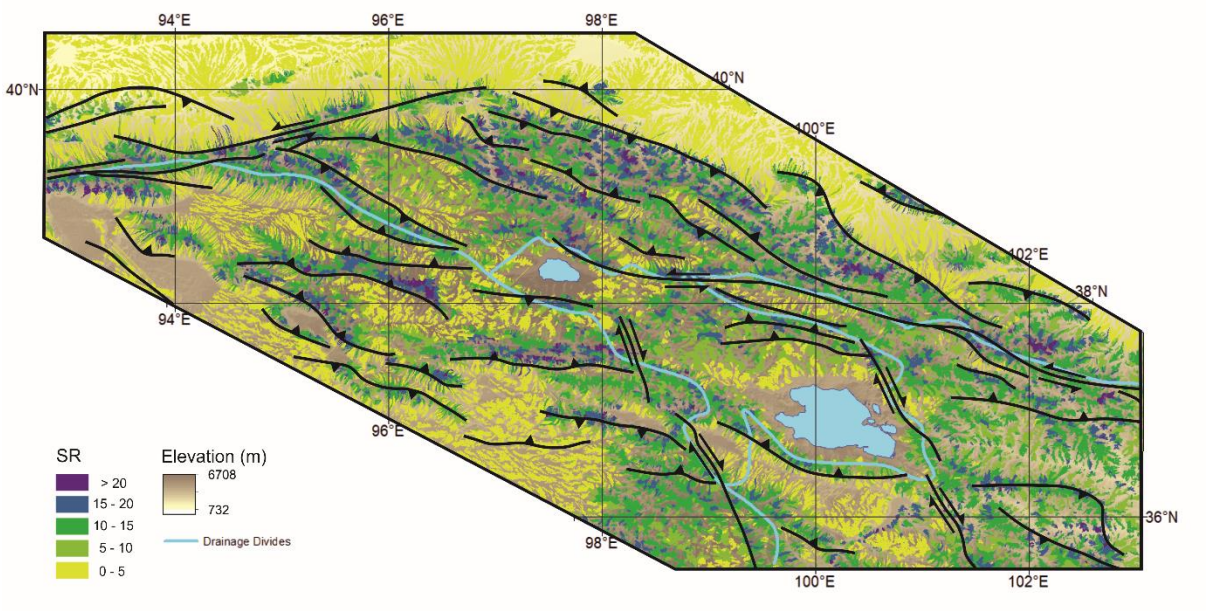

Figure 8. Surface roughness (SR - Mean: 9; Maximum; 33 Standard Deviation: 6) calculated for second Strahler order basins, shown with the major drainage divides and faults of the Qilian Shan. High SR values (>10) occur in the hangingwalls of active thrust faults and in the regions of major strike-slip faulting, such as the Altyn Tagh Fault. Lower SR values are present in the lowlands surrounding the Qilian Shan and also in the central, internally drained regions, where the rivers drain into the lakes.

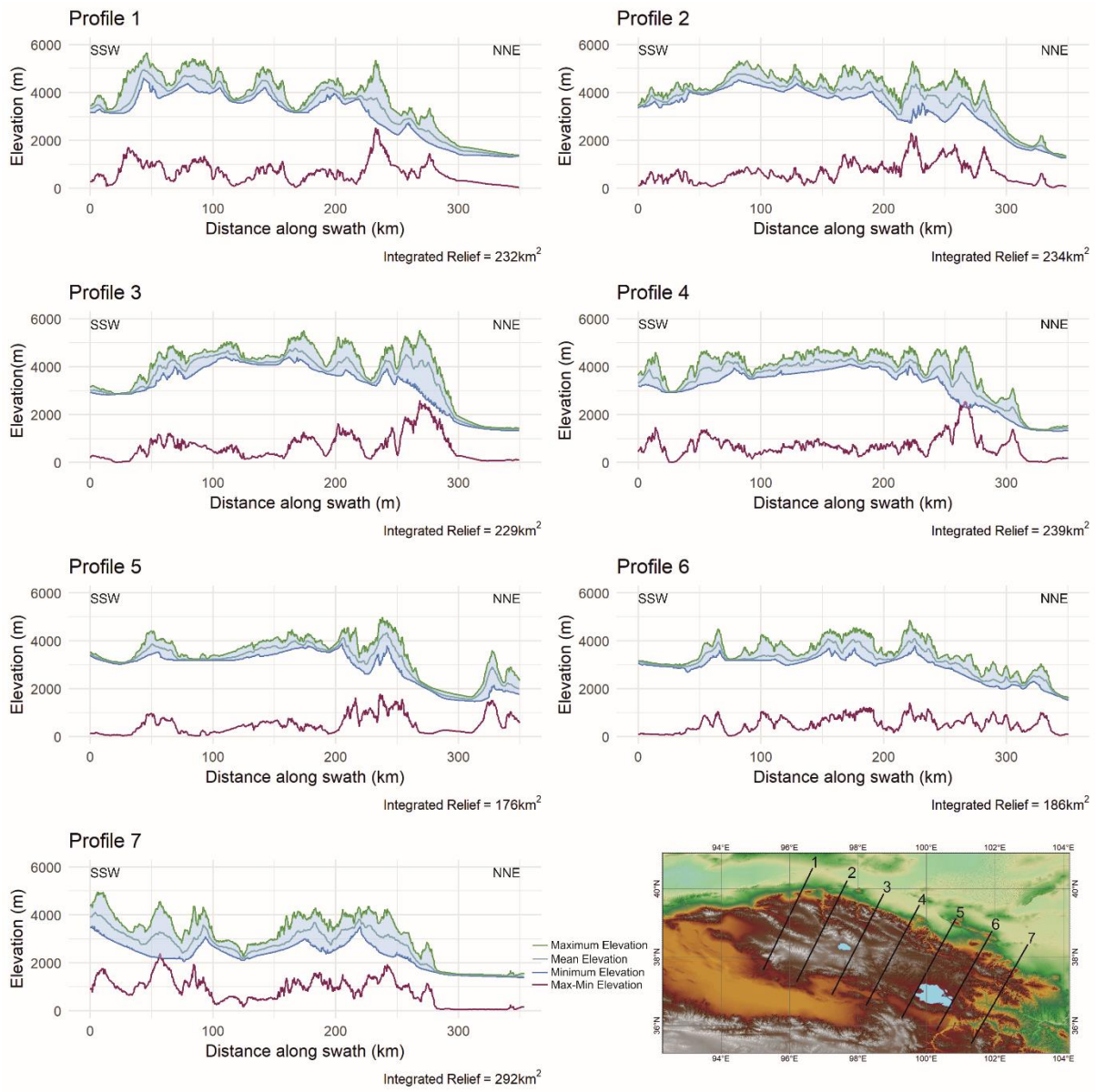

Figure 9. Swath profiles of elevation, each of total width 30 km and drawn from South West to North East. The location of the profiles is shown. The area between the maximum and minimum values (shaded and also shown in purple) is summed to give the integrated relief. Profiles 1-6 are orthogonal to the WNW-ESE trending thrust faults and near parallel to the rivers draining across the strike of the mountains. These show the plateau like morphology of the Qilian Shan. Profile 7 is orthogonal to the WNW-ESE trending thrust faults, but also orthogonal to the along strike rivers (Huangshui and Datong rivers) accounting for the more dissected swath profile, with the location of the river channel identifiable. Integrated relief is largely similar across the region.

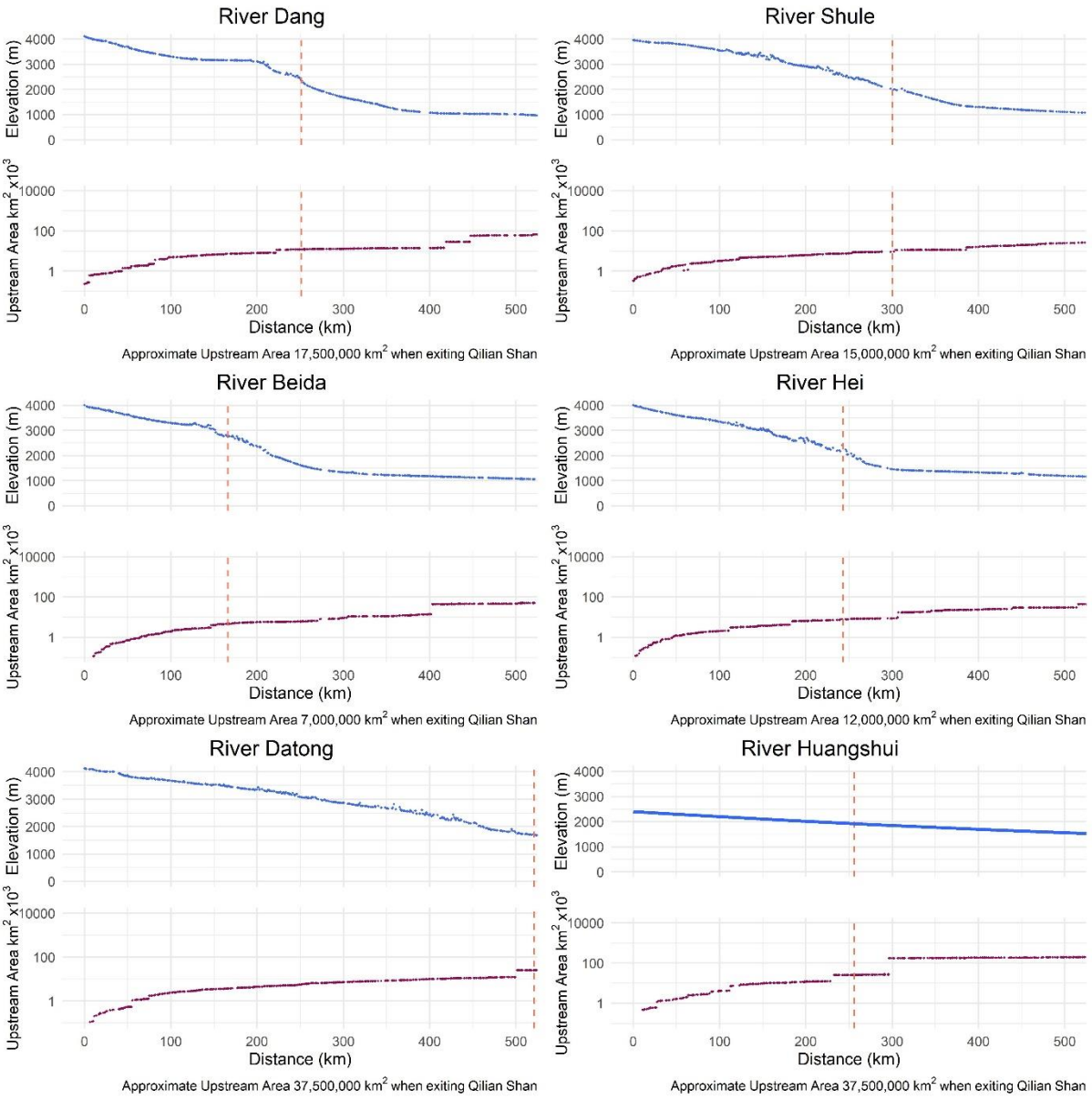

Figure 10: River profiles and upstream area of 6 major rivers draining the Qilian Shan, located in Figure 4. Upstream area is calculated by flow accumulation, multiplied by cell size. Vertical dashed line indicates the approximate extent of the Qilian Shan. The profiles show the stream profile morphology within the Qilian Shan to be largely similar. However the upstream areas vary from 7 million-17.5 million km^2 in the rivers flowing across the strike of the range (Dang, Shule, Beida and Hei) compared to 37.5 million km^2 for the range parallel tributaries of the Yellow River (Datong and Huangshui). This difference in upstream area may account for higher HI and SR values in the Yellow River tributaries.

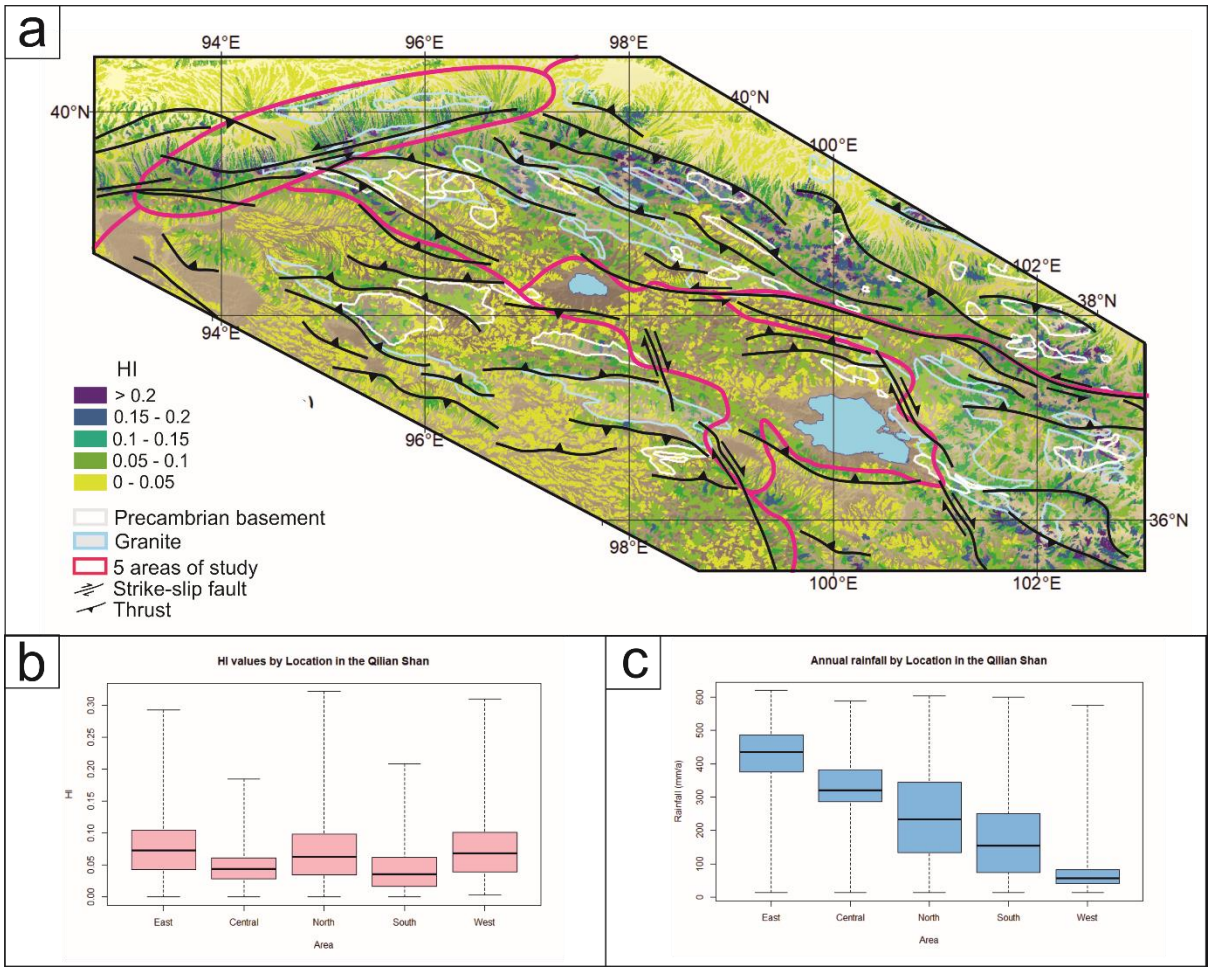

Figure 11.a. Areas of underlying crystalline basement and granites (Y. Zhang et al., 2017) are highlighted, overlain over the HI results. The underlying lithology appears to have no control on surface index values (see Supplementary Figure 12) as the same value distributions are found, regardless of lithology. b. Distribution of HI values across the 5 areas of the Qilian Shan. The box and whisker diagrams show the medians, interquartile ranges and range of data. c. Distribution of annual precipitation (mm) across the 5 areas of the Qilian Shan, shown as a box and whisker diagram. Precipitation decreases in general from East to West, with no systematic change in HI values.

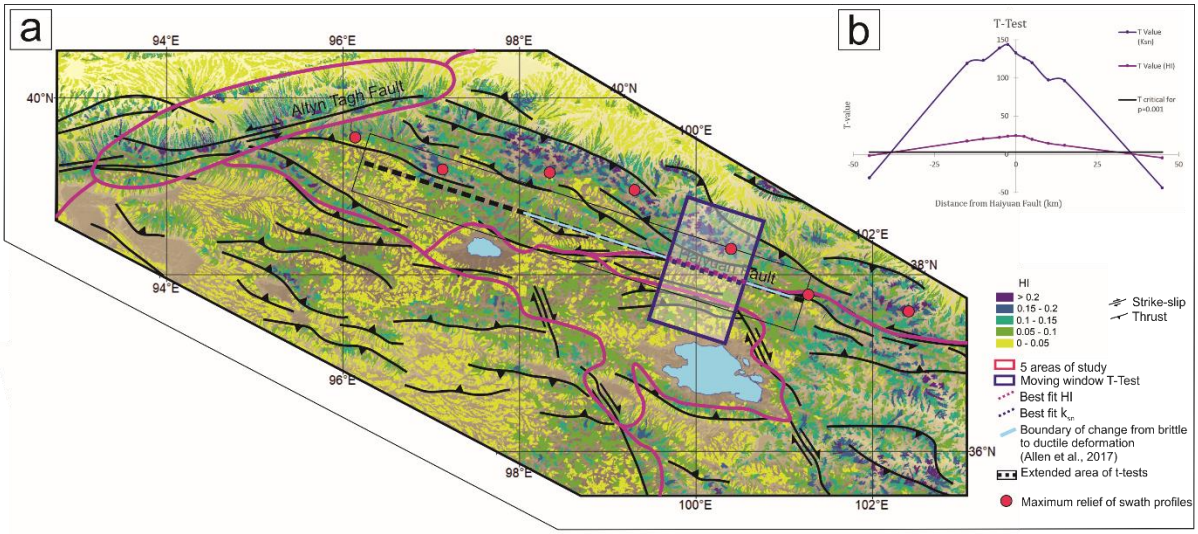

Figure 12. a. The moving window t-test in 12.b. is calculated over the area in the purple box and shows the greatest change in values to occur across the Haiyuan Fault. The pale blue line represents the width of the region of geodetic data used in the model of Allen et al., (2017), with the line representing a change from locked to creeping deformation on an underlying detachment. A second t-test across the width of the Qilian Shan, 550 km wide (black line) indicates that HI and K_{sn} is distinctly higher in the north of the region than the south, suggesting that the locked-creeping transition extends across the region. The location of maximum relief, calculated from the swath profiles in Figure 9, is shown to occur to the north of this black line. b. Results of the moving window t-test, showing the largest change in HI and K_{sn} to be within 2.5 km of the Haiyuan Fault, with the location of the change shown with the coloured lines in 12a.

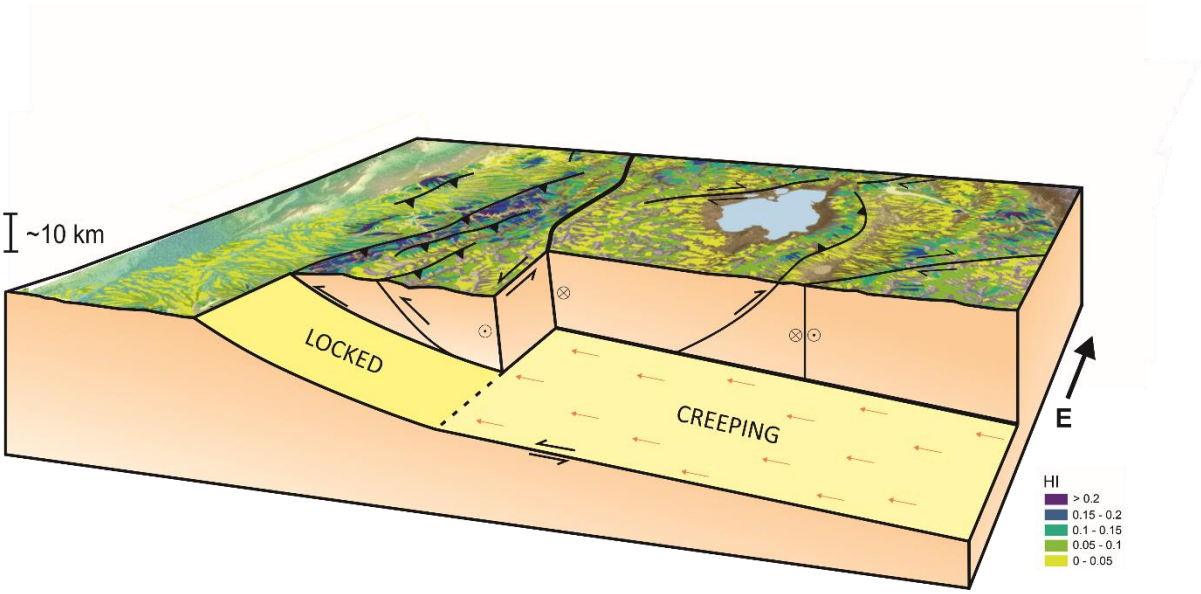

Figure 13. Schematic diagram showing inferred structure of Qilian Shan, underlain by a southwards-dipping detachment. A transition from locked to creeping behaviour is coincident with the location of the left-lateral Haiyuan Fault (Allen et al., 2017). This change is also coincident with the statistically significant change in our calculated surface indices, showing these results to be sensitive to underlying tectonics. The colours and values shown are the HI from Figure 5.